Hydrogenation of the Martian Core by Hydrated Mantle Minerals with Implications for the Early Dynamo

J. G. O'Rourke[1], S.-H. Shim[1]

[1]School of Earth and Space Exploration, Arizona State University, Tempe, AZ 85287

Corresponding author: Joseph G. O'Rourke (jgorourk@asu.edu)

Key Points:

- Mantle convection may deliver most of the primordial hydrogen from the mantle to the core via redox reaction at the core/mantle boundary.
- Hydrogen injected into the core could form a stratified layer and perhaps hinder the dynamo by sapping gravitational energy from convection.
- The NASA InSight mission or future geophysical platforms should provide key constraints on models of core hydrogenation.

Abstract

Mars lacks an internally generated magnetic field today. Crustal remanent magnetism and meteorites indicate that a dynamo existed after accretion but died roughly four billion years ago. Standard models rely on core/mantle heat flow dropping below the adiabatic limit for thermal convection in the core. However, rapid core cooling after the Noachian is favored instead to produce long-lived mantle plumes and magmatism at volcanic provinces such as Tharsis and Elysium. Hydrogenation of the core could resolve this apparent contradiction by impeding the dynamo while core/mantle heat flow is super-adiabatic. Here we present parameterized models for the rate at which mantle convection delivers hydrogen into the core. Our models suggest that most of the water that the mantle initially contained was effectively lost to the core. We predict that the mantle became increasingly iron-rich over time and a stratified layer awaits detection in the uppermost core—analogous to the E' layer atop Earth's core but likely thicker than alternative sources of stratification in the Martian core such as iron snow. Entraining buoyant, hydrogen-rich fluid downwards in the core subtracts gravitational energy from the total dissipation budget for the dynamo. The calculated fluxes of hydrogen are high enough to potentially reduce the lifetime of the dynamo by several hundred million years or longer relative to conventional model predictions. Future work should address the complicated interactions between the stratified, hydrogen-rich layer and convection in the underlying core.

Plain Language Summary

The demise of the Martian magnetic field roughly four billion years ago is one of the greatest mysteries in the Solar System. Many scientists believe that the temperature of the core is to blame. Producing the magnetic field requires a dynamo arising from convection in the core—like a boiling pot on a stove, but with molten iron instead of water. If the core started at a certain initial temperature, then its predicted cooling history agrees with ages of magnetized crust. However, models that attempt to explain the longevity of observed volcanism prefer an even hotter core. Here we study the amount of hydrogen that may enter the core through chemical reactions with minerals above the core that contain water. We found that the core may now contain most of the hydrogen that was initially located in the mantle. The predicted rates of hydrogen transport may strongly affect the energy budget for convection and the dynamo. Hydrogenation could never suppress a dynamo in other planets because they are too small (Mercury) or too large (Earth) for minerals containing significant amounts of water to contact the core. We suggest tests of our model for future laboratory experiments, simulations, and spacecraft missions.

1 Introduction

Mars is the only major planet besides Venus in our Solar System that now lacks a dynamo to generate a global magnetic field. However, a core-powered dynamo did exist for the first ~500 Myr of Martian history. Mars Global Surveyor discovered regions of strongly magnetized crust that formed before the Argyre and Hellas impact basins at ~3 to 4.1 Ga (e.g., Acuna et al., 1999; Connerney et al., 2004; Lillis et al., 2013; Moore & Bloxham, 2017). Remanent magnetization in the Martian meteorite ALH84001 also indicates that a dynamo existed at ~4 Ga (Weiss et al., 2002). The demise of a global magnetic field exposed atmospheric constituents such as water and carbon dioxide to rapid erosion by solar wind (e.g., Dehant et al., 2007), especially during storm events that typified the early evolution of the Sun (e.g., Jakosky et

al., 2015). After the dynamo disappeared, a large fraction of the primordial atmosphere was lost to space (e.g., Jakosky et al., 2017). The core of Mars is thus key to surface conditions.

Vigorous motions of conductive fluids in the core generate a dynamo. Assuming that thermal convection alone drives fluid motion yields a simple criterion for a dynamo: total heat flow across the core/mantle boundary (CMB) must exceed that transported by conduction up the adiabatic thermal gradient in the core (e.g., Stevenson, 2003, 2010). Simple parameterized models reliably predict an early dynamo if the core starts a few hundred degrees hotter than the lower mantle. They are fine-tuned so core/mantle heat flow becomes sub-adiabatic when the dynamo dies at ~4 Ga (e.g., Elkins-Tanton et al., 2005; Fraeman & Korenaga, 2010; Plesa et al., 2015; Roberts et al., 2009; Sandu & Kiefer, 2012; Williams & Nimmo, 2004). However, super-adiabatic heat flow across the CMB may persist for ≥1 Gyr longer using many plausible choices of parameters (e.g., Fraeman & Korenaga, 2010; Sandu & Kiefer, 2012; Williams & Nimmo, 2004). For example, adding primordial heat to the core increases the predicted longevity of the dynamo. The abundance of potassium in the core is typically limited to <100 ppm—in contrast to models of Earth's magnetic history that invoke >250–800 ppm (e.g., Driscoll & Bercovici, 2013; Nakagawa & Tackley, 2010, 2014). An inner core cannot nucleate because power from chemical buoyancy and latent heat would restart the dynamo (Williams & Nimmo, 2004). These restrictions on properties of the Martian interior have not been verified.

Allowing substantial core/mantle heat flow beyond the Noachian would violate standard models for the dynamo but help explain long-lived magmatism at large volcanic provinces. Stable mantle plumes are often invoked to form Tharsis and Elysium, which is most readily achieved in models featuring substantial heating of the mantle from below. Producing plumes and near-surface melting with negligible bottom heating requires additional complications such as layered mantle convection (Wenzel et al., 2004), adjusted rheology for the lower mantle (Li & Kiefer, 2007), and/or volatile-driven reduction of the mantle solidus (Kiefer & Li, 2016). In any case, more rapid heat flow across the CMB would help generate stable mantle plumes.

Models of planetary accretion and differentiation predict that the lower mantle initially contained some water. Depending on how many Mars-forming planetesimals originated from outer regions of the protoplanetary disk where volatiles easily condense, the primitive mantle may contain ~0.2–3 weight percent (wt%) of water (e.g., Breuer et al., 2016). Hydrous melting promotes efficient degassing of water from the upper mantle as proto-Mars grows, but the lower mantle may remain unmelted (Médard & Grove, 2006; Pommier et al., 2012). The water content of the upper mantle is ~200 ppm according to measurements of water in apatite inclusions from basaltic shergottites (Breuer et al., 2016; Taylor, 2013). The saturation limit of olivine is only a few times higher at ~1000 ppm. However, high-pressure polymorphs of olivine such as wadsleyite and ringwoodite may store up to ~2–3 wt% of water (Bolfan-Casanova, 2005; Fei et al., 2017; Pearson et al., 2014). Wadsleyite and ringwoodite are stable in Earth's transition zone at ~410 to 660 km depth and at equivalent pressures below ~1000 km depth in Mars. Interior structure models predict that the stability field of these polymorphs extends to the CMB, which should enable chemical reactions between the core and hydrated silicates.

Hydrogen is a likely constituent of the Martian core. Existing work typically treats the core as a two-component, iron/sulfur alloy (e.g., Khan et al., 2018; Plesa et al., 2018; Rivoldini et al., 2011). However, hydrogen is miscible in iron at extreme pressure/temperature conditions that are relevant to planetary accretion and the CMB at present day (Gudkova & Zharkov, 2004; Shibazaki et al., 2009, 2011). Hydrogen would tend to enter the core via redox reaction with

hydrated silicates in the lower mantle (Shibazaki et al., 2009): Fe (core) + H_2O (mantle) = 2H (core) + FeO (mantle). The partition coefficient for hydrogen between solid ringwoodite and liquid iron at pressures appropriate to the CMB was measured as ~9 (mass fraction) or ~26 (molar ratio), which implies that nearly all (~97% by number) of the hydrogen in silicates should partition into metal at thermodynamic equilibrium. Experiments have not yet constrained how composition and oxygen fugacity influence this partitioning behavior, as known for other elements (e.g., Davies et al., 2018; Fischer et al., 2015), or how partitioning may slow as the metal becomes hydrogen-rich. Ultimately, mantle dynamics govern the rate at which material is delivered to the relatively thin region above the CMB where redox reaction may occur.

The purpose of this study is to constrain the amount of hydrogen that entered the core over time. Previous research on this topic arrived at disparate conclusions. Shibazaki et al. (2009) proposed that nearly all hydrogen from the primordial mantle and putative oceans is now stored in the core. In contrast, Ruedas et al. (2013) argued that the rate of hydrogen transport across the CMB is negligible. We integrate a model for redox reaction at the CMB into a parametrized model for the thermochemical evolution of Mars that reproduces the observed dynamo history (Section 2). We conduct sensitivity analyses to report the range of possible scenarios given impactful uncertainties (Section 3). Adding hydrogen to the convecting core would sap gravitational energy from the dynamo. We explore the potential magnitude of this effect (Section 3.3), which previous studies have not considered, and outline future work required to reach definite conclusions (Section 4). In any case, hydrogenation of the core may change mantle composition over time and produce seismic structures that await detection today.

2 Theory and Numerical Methods

Figure 1 is a cartoon of the internal layers modeled in this study. Mars is differentiated into a silicate mantle and a metallic core. Wadsleyite and ringwoodite are stable below a depth of ~1000 km in the lower mantle where the water storage capacity is ~100 times larger than that in the upper mantle. Mantle convection always operates in the stagnant-lid regime. The lower mantle boundary layer (LMBL) controls the fluxes of heat and hydrogen out of and into the core, respectively. As hydrogen partitions across the CMB, a hydrogen-rich layer may grow at the top of the core. At early times, diffusive processes and/or convective entrainment may mix some hydrogen into the well-mixed core. Convection and the dynamo ceases in the core when the heat flow across the CMB falls below a critical value. Table 1 lists variables that track the evolution of the mantle, LMBL, and core in our models.

2.1 Hydrogen partitions across the CMB

Convective overturn of the LMBL controls the rate of heat loss from the core. Here we use a standard model of a thermal boundary layer (Stevenson et al., 1983):

$$Q_C = A_C k_M \Delta T_{BL}^{\frac{4}{3}} \mu_{BL}^{-\frac{1}{3}} \left(\frac{g \alpha_M \rho_M}{\kappa_M Ra_{crit}} \right)^{\frac{1}{3}}, \quad (1)$$

where A_C is the surface area of the CMB, k_M is the thermal conductivity of the lower mantle, g is the gravitational acceleration at the CMB, α_M is the thermal expansivity of the lower mantle, ρ_M is the density of the lower mantle, κ_M is the thermal diffusivity of the lower mantle, and Ra_{crit} is the critical Rayleigh number for convective instability. Table 2 lists values of all physical constants. The temperature contrast across the LMBL is $\Delta T_{BL} = T_C - T_L$ where T_C is the temperature of the core at the CMB and T_L is the temperature of the lower mantle above the

LMBL. Since the LMBL is ~100 km thick, $T_L = T_U + 275$ K where T_U is the potential temperature of the mantle and the adiabatic thermal gradient in the mantle is ~0.18 K/km (Filiberto, 2017). Dynamic viscosity in the LMBL obeys a Newtonian rheology (Fraeman & Korenaga, 2010):

$$\mu_M(T) = \mu_R \exp\left[\frac{E}{R}\left(\frac{1}{T} - \frac{1}{T_R}\right)\right], \tag{2}$$

where E is an activation energy, R is the universal gas constant, and μ_R and T_R are the reference viscosity and temperature, respectively. The average viscosity in the LMBL is $\mu_{BL} = \mu_M(T_C + 0.5\Delta T_{BL})$. The average thickness of the LMBL obeys Fourier's law (Stevenson et al., 1983):

$$\delta_{BL} = \frac{A_C k_M \Delta T_{BL}}{Q_C}. \tag{3}$$

Finally, the timescale for convective overturn of the LMBL is approximately that for thermal diffusion across its average thickness: $t_{ov} \sim \delta_{BL}^2/\kappa_M$ (Stevenson et al., 1983).

Geophysical data are insufficient to constrain ΔT_{BL} for Mars (e.g., Khan et al., 2018; Smrekar et al., 2019). Better constraints from seismology and mineral physics are available for Earth, but ΔT_{BL} is similarly uncertain within the range of ~500–1500 K today (e.g., Lay et al., 2008) and was possibly much larger in the past (e.g., Labrosse, 2015). Smaller values of ΔT_{BL} are expected for Mars relative to Earth since the amount of gravitational energy released during accretion and differentiation increases with planetary mass. However, an initial thermal contrast up to ~1000 K is still plausible for Mars (e.g., Ke & Solomatov, 2009; Stevenson, 2001). If $T_U \sim$ 1750 K and $T_L \sim$ 2025 K at early times (Filiberto, 2017), then ~3000 K is the upper bound on T_C.

Convective overturn of the LMBL also controls the rate of hydrogen transport across the CMB. Assuming the core is well-mixed, the change in the mass fraction of hydrogen across the LMBL is expressed as $\Delta C_{H,BL} \sim C_{H,LM} - C_{H,C}/D^H_{Fe/rw}$ where $C_{H,LM}$ and $C_{H,C}$ are the average mass fractions of hydrogen in the lower mantle and core, respectively. The partition coefficient for hydrogen is $D^H_{Fe/rw} = X^H_{Fe}/X^{\mathrm{H}}_{rw}$, where X^H_{Fe} and X^{H}_{rw} are the mass fractions of hydrogen in metal and ringwoodite, respectively. At any time, the downward mass flux of hydrogen into the core obeys Fick's law (Turcotte & Schubert, 2002):

$$\left(\frac{dM_H}{dt}\right)_{cmb} = A_C \rho_M D_{H,BL}\left(\frac{\Delta C_{H,BL}}{h}\right), \tag{4}$$

where $D_{H,BL}$ is the effective diffusivity of hydrogen at the base of the LMBL and h is height above the CMB. Adapting the standard solution for diffusion through a semi-infinite half-space, $h \sim (\pi D_{H,BL} t)^{1/2}$ (Turcotte & Schubert, 2002). Averaging Eq. 4 over t_{ov} yields the total mass flux of hydrogen from the mantle into the core:

$$\left(\frac{dM_H}{dt}\right)_{cmb} = 2A_C \rho_M \Delta C_{H,BL}\left(\frac{D_{H,BL}}{\pi t_{ov}}\right)^{\frac{1}{2}}. \tag{5}$$

This equation is identical to the expression obtained by differentiating Eq. A.3 from Ruedas et al. (2013) with one exception: they used the time after accretion (t) instead of t_{ov}, which can underestimate the mass flux at later times because $t_{ov} \sim$ 1 Gyr.

Constraining the effective value of $D_{H,BL}$ within ~4–5 orders of magnitude is difficult. The diffusivity of hydrogen in solid wadsleyite and ringwoodite has been estimated to range from ~10^{-10}–10^{-5} m^2/s at the temperature/pressure conditions of the lower mantle of Mars or Earth's transition zone (e.g., Bercovici & Karato, 2003). Figure S1 illustrates that recent simulations (Caracas & Panero, 2017) and experiments (Hae et al., 2006; Sun et al., 2015) favor values towards the middle of this range, e.g., ~10^{-8}–10^{-7} m^2/s. However, partial melting of the basal mantle may speed the transport of hydrogen through the LMBL. Especially at early times, the core was plausibly several hundred degrees hotter than the dry and wet solidi in the mantle. The dry solidus of the Martian mantle is ~2358 K at 19 GPa (Duncan et al., 2018), which decreases by ~180 K to ~2178 K if 2 wt% H_2O is added (e.g., Litasov & Ohtani, 2007). Iron hydride melts at these temperatures (Sakamaki et al., 2009). Hydrous magma could have neutral or negative buoyancy at the base of the Martian mantle as in Earth's transition zone (e.g., Sakamaki, 2017; Sakamaki et al., 2006). Two-phase flow could chemically refresh the CMB with hydrogen-rich fluid at timescales shorter than t_{ov} and with concentration gradients across the CMB greater than $\Delta C_{H,BL}$ locally. We consider values of $D_{H,BL}$ up to ~2 orders-of-magnitude larger than the values from Fig. S1 to account heuristically for enhanced mass transport with partial melting.

Diffusion of hydrogen in the liquid core is much faster than in solid silicates. Our nominal value for its diffusivity in the core is $D_{H,C} = 1.2 \times 10^{-7}$ m^2/s , which is twenty times the diffusivity of oxygen in liquid iron at 20 GPa and 2000 K inferred from recent experiments (Posner et al., 2017). The plausible range for $D_{H,C}$ extends from ~1.4×10^{-7} m^2/s as measured at ~1873 K and ambient pressure (Depuydt & Parlee, 1972) to ~8×10^{-8} m^2/s for Earth's core at 4400 K and 130 GPa from first-principles calculations (Umemoto & Hirose, 2015).

2.2 Towards a thermochemical history of Mars

Parameterized models provide insights into the partitioning of hydrogen between the surface, mantle, and core over geologic time. We adapted a previously published model (Fraeman & Korenaga, 2010), which features a novel parametrization of stagnant-lid convection with dehydration stiffening and compositional buoyancy (Korenaga, 2009). These factors tend to slow mantle cooling over time and can lead to non-monotonic core cooling if the core starts relatively cold (i.e., $T_C \leq 2300$ K). Plesa & Breuer (2014) provide important context and a contrasting view on dehydration stiffening. Readers are referred to Fraeman & Korenaga (2010) for the full description of the model. All details are preserved without modification unless noted.

Our focus on hydrogenation of the core complements earlier studies on the degassing of water from the mantle to the surface. Degassed hydrogen may enter the atmosphere and then become lost to space. These processes were not modeled in detail because atmospheric conditions (i.e., surface temperature) probably do not provoke transitions in mantle or core dynamics for Mars, unlike Venus (e.g., O'Rourke et al., 2018). The global mass budget of hydrogen is $M_{PM}^H = M_{SM}^H - M_S^H - M_C^H$, where subscripts *PM*, *SM*, *S*, and *C* respectively refer to the primitive and source mantle, surface, and core. The mass of hydrogen transferred from the source mantle into the core is $(dM_H/dt)_{cmb}\Delta t$, where $\Delta t = 1$ Myr is the duration of each time step. The flux of hydrogen degassed to the surface as water in each time step is $\Delta M_{SM}^H = \rho_M C_{W,UM} f_H \Delta V_{proc}$, where $C_{W,UM}$ is the mass fraction of water in the upper mantle, f_H is the mass fraction of hydrogen in water, and ΔV_{proc} is the volume of mantle that undergoes partial melting and produces crust (Fraeman & Korenaga, 2010). Source regions for surface magmatism were

drier than the lower mantle because olivine has a relatively low water storage capacity. The mass fraction of water in the upper mantle is $C_{W,UM} << C_{H,LM}/f_H$. Degassed water was never recycled in these models although burial of hydrated mafic crust may provide a pathway for volatile transport into the Martian interior (Wade et al., 2017).

2.3 Core dynamics

We updated an older model of the core (Fraeman & Korenaga, 2010; Stevenson et al., 1983) to better compute the thermodynamic budget for convection and a dynamo.

2.3.1 Radial structure of the core

Following previous studies of Earth (Labrosse, 2015) and Venus (O'Rourke et al., 2018), one fiducial structure for the core of Mars was used because structural parameters are insensitive to small changes in size and composition. As shown in Figure S2, the density profile was fit to a fourth-order polynomial (Labrosse, 2015):

$$\rho(r) = \rho_0 \left[1 - \left(\frac{r}{L_p}\right)^2 - A_p \left(\frac{r}{L_p}\right)^4\right], \quad (6)$$

where r is radial distance from the center of the core, $A_p = 0.5K' - 1.3$, and $L_p = [3K/(2\pi G\rho_0^2]^{1/2}$ is a characteristic length scale. The Supporting Information contains equations of state used to derive density from pressure, temperature, and composition. The adiabatic temperature profile is

$$T_a(r) = T_0 \left[1 - \left(\frac{r}{L_p}\right)^2 - A_p \left(\frac{r}{L_p}\right)^4\right]^{\gamma}, \quad (7)$$

where T_0 is the temperature at the center of the core and γ is the Grüneisen parameter. Once convection in the core stops at ~500 Myr, the assumption that density and temperature are adiabatic becomes invalid. However, Eq. 6 and 7 still provide adequate approximations of the bulk structure of the core. Deviations from adiabatic gradients that suppress convection in the core are small relative to the radial density profile. That is, A_p, L_p, K', and K are fixed constants. For example, assuming that the core is isothermal instead of adiabatic changes their best-fit values by ~10%, which is less than or similar to the uncertainties on other physical parameters. A stratified, hydrogen-rich layer may form at the top of the core while the well-mixed core remains convective. The buoyancy frequency associated with chemical stratification is

$$N_H = \left[-g\alpha_H \left(\frac{dC_H}{dz}\right)\right]^{\frac{1}{2}}. \quad (8)$$

The coefficient of compositional expansion for hydrogen in iron is $\alpha_H = -1/\rho(\partial\rho/\partial C_H) \sim [(55.845 + 1.008)/1.008][(\rho_{Fe} - \rho_{FeH})/\rho_{Fe}] \sim 7.96$ at 20 GPa and 1800 K, where ρ_{Fe} is the density of pure iron and ρ_{FeH} is the density of iron hydride (Supporting Information). For estimates using Eq. 8, we assume that the average concentration of hydrogen is zero in the well-mixed core and $C_{H,SL}$ in the stratified layer so $dC_H/dz \sim -2C_{H,SL}/h_{SL}$, where h_{SL} is the thickness of the stratified layer. Decreasing the radius of the convecting region to accommodate stratification below the CMB does not strongly affect the bulk energy and dissipation budgets for the well-mixed core (i.e., the total dissipation increases by ~12% if the radius is lowered by ~130 km).

We derive our fiducial structure for a core with any bulk composition between two endmembers: 12 wt% S, 1 wt% H, and 87 wt% Fe versus 16 wt% S, 0 wt% H, and 84 wt% Fe. The mass of hydrogen delivered into the core after accretion is much smaller than uncertainties

on the bulk composition. Crucially, the radius of the core (~1758 km), the core mass fraction (~23.7%), and the pressure at the CMB (~19 GPa) are all consistent with the observed mass, moment of inertia, and tidal Love number of Mars (Khan et al., 2018; Rivoldini et al., 2011).

2.3.2 Energy sources and sinks in the core

Any dynamo requires constant sources of power to survive over geologic time because its free decay time is only ~10^4 years (Stevenson, 2003, 2010). In reality, the total dissipation must exceed non-zero Ohmic losses that are poorly constrained (e.g., Christensen, 2010; Stelzer & Jackson, 2013). For simplicity in this study, vigorous convection and thus a dynamo is assumed to exist for any positive dissipation. Integrating terms over the core determines the global energy budget. Two heat sources and one heat sink were considered:

$$Q_C = Q_S + Q_R - Q_H, \tag{9}$$

where Q_S is secular cooling, Q_R is radiogenic heating, and Q_H is gravitational energy associated with hydrogenation. Positive Q_H corresponds to downward entrainment of hydrogen-rich fluid, meaning that hydrogen chemically diffuses into the downwelling flow and/or fluid dynamical processes such as penetrative convection mechanically mix hydrogen into the convecting system. Redistributing buoyant material throughout the convective system spends gravitational energy and thus reduces the vigor of convection. In contrast, models of Earth's core include sources of gravitational energy such as the exclusion of light elements from the growing inner core (Labrosse, 2015) and the precipitation of MgO and/or SiO_2 at the top of the core (Badro et al., 2016; Hirose et al., 2017; O'Rourke & Stevenson, 2016). Unlike Earth, Mars probably did not accrete and differentiate under sufficiently high temperatures and pressures for substantial amounts of Mg, Si, and/or O to partition into the core (Brennan et al., 2019).

Our polynomial model for the radial structure of the core permits analytic expressions for each term in Eq. 9. For example, secular cooling secular cooling of the well-mixed core is proportional to the cooling rate of the well-mixed core as $Q_S = \tilde{Q}_S(\mathrm{d}T_C/\mathrm{d}t)$, where

$$\tilde{Q}_S = 4\pi\rho_0 C_p L_p^3 f_c\left(\frac{R_C}{L_p}, \gamma\right)\left(\frac{T_0}{3T_C}\right) \tag{10}$$

and f_c is a useful function with $f_c(R_C/L_p,\gamma) = 0.0184$ (Labrosse, 2015) and C_p is the specific heat of the core. The change in gravitational energy from redistributing a thin layer of hydrogen (e.g., the convective boundary layer below the CMB) uniformly throughout the well-mixed core is

$$Q_H = \int_{wm} \frac{\phi\rho\alpha_H}{M_C}\left(\frac{dM_H}{dt}\right) dV = \frac{8}{3}\pi^2 G\rho_0^2 L_p^5 \alpha_H f_\gamma\left(\frac{R_C}{L_p}\right)\left[\frac{\left(\frac{dM_H}{dt}\right)_{wm}}{M_C}\right]. \tag{11}$$

The gravitational potential (ϕ) and other terms are integrated over the volume (V) of the well-mixed core (wm). Here M_C is the total mass of the core and $(\mathrm{d}M_H/\mathrm{d}t)_{wm}$ is the mass flux of hydrogen that convection accommodates. However, we assumed that $(\mathrm{d}M_H/\mathrm{d}t)_{wm}$ and Q_H are negligibly small except Section 3.3 discusses the possibility that $(\mathrm{d}M_H/\mathrm{d}t)_{wm} = (\mathrm{d}M_H/\mathrm{d}t)_{cmb}$ in steady state. We defined another useful function:

$$f_\gamma(x) = x^3\left[-\frac{\Gamma}{3} + \frac{(1+\Gamma)\mathrm{x}^2}{5} + \frac{A_p(\Gamma - 1.3)\mathrm{x}^4}{7}\right], \tag{12}$$

where $\Gamma = (R_C/L_p)^2[1 - 0.3(R_C/L_p)^2]$. We calculated Q_R with potassium-40 as the only source of radiogenic heating in the core (Supporting Information). Uranium and thorium are incompatible

in iron alloys at relevant pressure/temperature conditions (Blanchard et al., 2017; Chidester et al., 2017). Finally, we calculated the absolute cooling rate of the core as

$$\frac{dT_C}{dt} = \frac{Q_C - Q_R + Q_H}{\tilde{Q}_S}. \tag{13}$$

This formulation assumes that the entire core is well-mixed. Including a thick, stable layer would necessitate using a reduced total heat flow ($<Q_C$ since stratification is a heat sink) in Eq. 9 and the actual radius of the well-mixed core ($<R_C$) in Eq. 10 and 11.

2.3.3 Total dissipation available for a dynamo

Using the energy balance, we computed the total dissipation available to power any magnetic dynamo (Labrosse, 2015; O'Rourke et al., 2017, 2018):

$$\Phi = \left(\frac{T_D(T_S - T_C)}{T_S T_C}\right) Q_S + \left(\frac{T_D - T_C}{T_C}\right) Q_R - \left(\frac{T_D}{T_C}\right) Q_H - T_D E_K, \tag{14}$$

where T_D is the effective temperature at which uniformly-distributed dissipation occurs—close to the average temperature in the well-mixed core. Dissipations associated with secular cooling and radiogenic heating—but not hydrogenation—are penalized by Carnot-like efficiency terms. The effective temperature of dissipation for secular cooling (T_S) is slightly larger than T_D because the associated buoyancy flux is generated near the CMB (Labrosse, 2015). The adiabatic heat flow is simply $Q_{ad} = [T_C T_S/(T_S - T_C)]E_K$. Here E_K is an entropy sink arising from thermal conductivity, which vanishes from the energy balance because it only incorporates heat that is conducted internally and remains inside the core. The Supporting Information explains how to calculate these terms. We assumed that viscous dissipation and barodiffusion are negligible although they may detract from the total dissipation (Gubbins & Davies, 2013). Finally, we obtain a lower bound on the total heat flow out of the well-mixed core required to sustain a dynamo by rearranging Eq. 9 and 14 with $\Phi = 0$ W:

$$Q_{crit} = \left(\frac{T_C}{T_S - T_C}\right) Q_H + \left(\frac{T_C(T_S - T_D)}{T_D(T_S - T_C)}\right) Q_R + \left(\frac{T_C T_S}{T_S - T_C}\right) E_K. \tag{15}$$

That is, a dynamo may exist if $Q_C > Q_{crit}$. The normal criterion for thermal convection is $Q_C > Q_{ad}$, but $Q_{crit} \geq Q_{ad}$ by definition. We adjust the thermal conductivity of the core to match the observed lifetime of the Martian dynamo in postprocessing for each model. Rearranging Eq. 14, the condition for a dynamo is

$$E_K < \left(\frac{1}{T_C} - \frac{1}{T_S}\right) Q_S + \left(\frac{1}{T_C} - \frac{1}{T_D}\right) Q_R - \frac{Q_H}{T_C}. \tag{16}$$

Thermal conductivity is directly proportional to E_K (Supporting Information). The "critical conductivity" for each model is the value of k_c that yields $\Phi = 0$ W at 500 Myr. Because Q_C decreases monotonically in these models, the dynamo is never predicted to restart later.

2.4 Initial conditions and sensitivity analyses

One set of initial conditions was chosen to generate a representative model. The potential temperature of the mantle was initially $T_U = 1750$ K (Filiberto, 2017). For the mantle rheology described in Section 2.4 of Fraeman & Korenaga (2010), the reference viscosity was 10^{20} Pa s and the viscosity contrast between wet and dry mantle was 5, which leads to some dehydration

stiffening in the lithosphere. As shown in Fig. 1, the mantle above ~1000 km depth contains "dry" minerals (e.g., olivine, pyroxene, and garnet), which are assumed to host initially 200 ppm of water. In contrast, we assumed that wadsleyite and ringwoodite compose ~60 wt% of the lower mantle and store 0.6 wt% of water at early times so $C_{H,LM} = 4 \times 10^{-4}$ (i.e., 0.37 wt% of water or 400 ppm of hydrogen). The initial temperature and potassium content of the core are T_C = 2700 K and $[K]_C$ = 80 ppm, respectively. Initially, the core contained no hydrogen. A reference viscosity of $\mu_R = 10^{23}$ Pa s without dehydration stiffening was used for the LMBL. Using a critical conductivity of k_c = 53 W/m/K ensured that the dynamo died at ~500 Myr.

Sensitivity analyses were performed to investigate the effects of five parameters that govern the evolution of the core and dynamo. Specifically, we ran models with $D_{H,BL} = 10^{-5}$, 10^{-6}, 10^{-7}, and 10^{-8} m^2/s; $C_{H,LM} = 4 \times 10^{-4}$ and 10^{-3}; $[K]_C$ = 0 and 80 ppm; $T_C(0)$ = 2300, 2500, 2700, and 2900 K; and $\mu_R = 10^{22}$, 10^{23}, and 10^{24} Pa s. In total, 192 models covered all permutations of these input parameters. We tracked three key outputs for each model: the critical conductivity, the final mass of hydrogen sequestered in the core, and the total mass flux of hydrogen transported across the CMB at 500 Myr. Table S2 lists the inputs and outputs for all models.

3 Results

3.1 Representative model for the evolution of Mars

Figure 2 shows one parameterized model for the long-term history of Mars with hydrogenation of the core but assuming Q_H is zero. In general, the evolution of the mantle and surface was at least roughly consistent with previous studies (Fraeman & Korenaga, 2010). The potential temperature of the mantle is T_U ~ 1676 K now compared to ~1875 K at 4 Gyr ago and 1750 K initially (Fig. 2a), which is within ~100 K of those temperatures predicted from petrologic studies (Filiberto, 2017) and dynamical simulations (Plesa et al., 2018). Likewise, the surface heat flow is ~18.4 mW/m^2 at present day (Fig. 2b) compared to estimates of ~15 mW/m^2 for the north polar cap (Phillips et al., 2008) and ~21 mW/m^2 on average from simulations (Plesa et al., 2015). Most crustal production occurs during the first ~1 Gyr of Martian history (Fig. 3c). The average crustal thickness is ~47 km today, which is consistent with gravity and topography data (e.g., Wieczorek & Zuber, 2004). In general, these outputs depend almost exclusively on the initial temperature of the mantle and the rheology and melting behavior of the stagnant lid. Heat flow from the core contributes ~10% or less of the energy budget for the mantle, so even extreme initial conditions for the core do not strongly affect modern properties of the mantle and crust.

Heat flow from the core declined monotonically in this representative model. The thermal contrast across the LMBL was $\Delta T_{BL} = T_C - T_L$ = 2700 K – 2025 K = 675 K initially and ~365 K at present (Fig. 2a). Average viscosity in the LMBL ranged from ~$10^{19.7}$ to $10^{20.6}$ Pa s with a minimum at ~500 Myr when the mantle reached its maximum temperatures (Fig. 2d), which is consistent with a large pressure-dependence of viscosity yielding higher viscosity in the lower versus upper mantle (Plesa et al., 2018). The timescale for convective overturn of the LMBL was <1 Gyr until <1 Gyr ago (Fig. 2e), meaning that instead using the age of Mars in Eq. 5 (Ruedas et al., 2013) would underestimate the rate of hydrogen partitioning into the core.

Hydrogen was lost through the top and bottom boundaries of the mantle at comparable rates (Fig. 2f). Water loss to the surface paralleled crustal production. Overall, ~19% and 59% of the water in the primitive mantle was lost to the surface and core, respectively. The abundances of hydrogen in the core and FeO in the mantle increased by ~218 ppm and ~0.23 wt%, respectively. At present, the hydrogen content of the core is less than the equilibrium value of

~792 ppm (i.e., $C_{H,LM}D^{H}_{Fe/rw}$ with 88 ppm of hydrogen remaining in the basal mantle) if the core is well-mixed. In general, hydrogen loss to the core continues while Q_C remains non-zero.

Figure 2h and 2i show the heat and dissipation budgets for the core, respectively. Secular cooling and radiogenic heating were initially comparable, but $Q_C \sim Q_S$ in recent times since most potassium-40 in the core has decayed. Using the critical conductivity, $Q_C = Q_{ad} \sim 0.75$ TW at 500 Myr so thermal convection in the core would shut down at that time and the dynamo would dissipate shortly thereafter. From 500 Myr to 3 Gyr, Q_C declined at an average rate of ~0.14 TW per 1 Gyr. Fine-tuning of Q_{ad}, which is directly proportional to thermal conductivity, was required to reproduce the magnetic history. If the thermal conductivity of the core were reduced to ~40 or 30 W/m/K, which are plausible values (Deng et al., 2013), then the predicted lifetime of the dynamo from this model would have been ~1.7 or 3.1 Gyr, respectively.

Figure 3a compares the history of hydrogenation from our model to scenarios from Shibazaki et al. (2009) and Ruedas et al. (2013). Shibazaki et al. (2009) considered the fate of a putative Late Hesperian/Early Amazonian ocean with a mass of ~10^{20} kg (Boyce et al., 2005). They used a simple scaling relationship to posit that subduction transported 1.8×10^{20} kg of water through the mantle to the CMB, where 97 mol% (1.9×10^{19} kg) of the hydrogen dissolved into the core (~95% efficiency by mass). Our model has 5×10^{20} kg of water in the primitive mantle and ends with 3.4×10^{19} kg of hydrogen in the core, meaning that mantle convection delivers hydrated silicates to the CMB with ~64% efficiency. If we used the expression from Ruedas et al. (2013) and the diffusivity of hydrogen in solid ringwoodite (Hae et al., 2006), then only 4.5×10^{18} kg of hydrogen enters the core (~9% efficiency). Using t_{ov} instead of t in Eq. 5 roughly doubles the predicted efficiency of mantle convection (e.g., to ~20% from 9%). Assuming that partial melting in the LMBL increased the effective diffusivity of hydrogen by ~1–2 orders of magnitude contributed an additional factor of ~3 to the transport rates.

Figure 3b illustrates the stability of a hydrogen-rich layer at the top of the core. Our model assumed that the core remained well-mixed, so the growth of a stratified layer was not computed directly. Future simulations are needed to predict the actual magnitude and extent of stratification (e.g., Bouffard et al., 2017). A simple estimate for the thickness of a hydrogen-rich layer at present is ~$(D_{H,C} \times 4.5\ \mathrm{Gyr})^{1/2} \sim 130$ km. Double-diffusive processes could extend the stratification (Turner, 1973), but penetrative convection could erode it (Dietrich & Wicht, 2018). Models with alternative sources of stratification such as iron snow in a sulfur-rich core predict ~100 km of stratification (Davies & Pommier, 2018). If the chemical gradient is linear across the stratified layer, then our reference model predicts $N_H \sim 9.5\Omega_M \sim 6.7 \times 10^{-4}$ Hz. A layer thickness of 400 km and the mass flux predicted by Ruedas et al. (2013) could provide a lower bound for the stability of the hydrogen-rich layer. The buoyancy frequency is then at least $N_H \sim 1.2\Omega_M$, which indicates that rotation is important to hydrogen transport within the core.

3.2 Sensitivity of parameterized models to initial conditions

Figure 4 shows how initial conditions affected the total mass of hydrogen delivered into the core over geologic time. In general, $C_{H,LM}$ and $D_{H,BL}$ control the amount of hydrogen that leaves the mantle while the other three parameters (T_C, $[\mathrm{K}]_C$, and μ_R) govern the critical conductivity. Here the total mass of hydrogen was converted into an equivalent depth of surface water (e.g., 1.6×10^{19} kg of hydrogen corresponds to a ~1-km-thick global ocean). If $C_{H,LM} = 4 \times 10^{-4}$, then $D_{H,BL} = 10^{-5}$, 10^{-6}, 10^{-7}, and 10^{-8} m^2/s translate to ~0.3, 0.9, 2.0, and 3.0 km of water lost to the core, respectively (Fig. 4a). Increasing $C_{H,LM}$ to 10^{-3} proportionally increased the

predicted water loss to ~0.9, 2.4, 5.2, and 7.3 km (Fig. 4b). The maximum change in the FeO content of the mantle over 4.5 Gyr was ~0.8 wt% if ~10^{21} kg (~7.3 km) of water in the mantle reacted with the core. Adding heat to the core increased its cooling rate. Specifically, a ~100 K increase in T_C raised the critical conductivity by ~20–30 W/m/K. Likewise, setting $[K]_C = 80$ versus 0 ppm increased the critical conductivity by ~5–15 W/m/K. Finally, increasing the reference viscosity reduced the variability of CMB heat flow. When Q_C declines relatively slowly over time, small changes to Q_{ad} yielded dramatic differences in the predicted lifetime of the dynamo. High viscosity also reduced Q_C in an absolute sense via Eq. 1. Models with $\mu_R = 10^{24}$ Pa s had critical conductivities from ~7–47 W/m/K. In contrast, models with $\mu_R = 10^{22}$ Pa s featured a broad range of critical conductivities: ~15–112 W/m/K. Overall, fine-tuning was required to reproduce ~500 Myr as the lifetime of the Martian dynamo. Many models predicted that the dynamo would have lasted into the Hesperian or even Amazonian.

3.3 Potential energetic impact of hydrogenation

Convection may entrain a substantial fraction of the hydrogen that crosses the CMB into the well-mixed region of the core. We assumed $Q_H = 0$ W so $(dM_H/dt)_{wm} = 0$ kg/s to calculate the critical conductivity, implicitly implying that hydrogen transported into the core (e.g., when $[dM_H/dt]_{cmb} > 0$ kg/s) remained in a stratified layer below the CMB. In reality, diffusion must carry some hydrogen into the convective region. Double-diffusive processes could vastly increase the rate of mass transfer (Leconte & Chabrier, 2012; Turner, 1973). Numerical simulations of rapidly rotating fluid (e.g., with $N_H \sim \Omega_M$) suggest that convective flows may penetrate far into the stratified layer (Dietrich & Wicht, 2018). Penetrative convection could destroy any double-diffusive interfaces but would also mix hydrogen-rich fluid into the convecting system. Rearranging Eq. 11 and 14 provides an upper limit on the mass flux of hydrogen that convection could accommodate while maintaining positive dissipation ($\Phi > 0$ W):

$$\left(\frac{dM_H}{dt}\right)_{wm} < \frac{3M_C\left[\left(\frac{T_S}{T_C}-1\right)Q_C - \left(\frac{T_S}{T_D}-1\right)Q_R - T_S E_K\right]}{8\pi^2 G\rho_0^2 L_p^5 \alpha_H f_\gamma \left(\frac{R_C}{L_p}\right)}. \quad (17)$$

Figure 5 illustrates this limit for our representative model where the approximate relation is $(dM_H/dt)_{wm} < 5000$ kg/s × $\{Q_C - (0.5\text{ TW}) \times [k_c / (40\text{ W/m/K})]\}$ / (1 TW). If the mass flux across the CMB exceeds this limit, then the entire core cannot remain chemically homogenous. One possibility is that most hydrogen remains in a stratified layer, which would not detract from the dissipation budget for the well-mixed core if the layer remains relatively thin and weakly stratified. That is, the terms in Equation 14 would be integrated from the center of the core to the bottom of the stratified layer. Alternatively, the density gradient at the top of the well-mixed core could resist convection (e.g., the positive buoyancy from hydrogenation would outweigh the negative buoyancy from cooling). Without a source of compositional buoyancy deeper down such as an inner core, convection in the well-mixed core could cease and the thermal gradient would relax by conduction towards an isothermal state. Overall, the general problem of convection under the influence of rotation, magnetic fields, and countervailing sources of buoyancy is complex. Whether fast rates of hydrogenation would stop convection is an open question that we intend to explore in future work with numerical simulations.

Hydrogenation of the core may explain why models overestimate the longevity of the dynamo if convective mixing is efficient. Critically, decreasing the model conductivity by 10

W/m/K increases the predicted lifetime of the dynamo by ~1 Gyr. Downward entrainment of buoyant fluid in the convecting core would lower the critical conductivity. A plausible range for the actual conductivity is ~20–60 W/m/K (Davies & Pommier, 2018; Deng et al., 2013; Williams & Nimmo, 2004). A model with a critical conductivity of ~80 W/m/K thus over-predicts the dynamo lifetime by ≥2 Gyr. This lower bound only excludes 40 models with $[K]_C = 0$ ppm and/or $T_C = 2300$ K. However, 48 models returned critical conductivities >60 W/m/K. A simple relation for the decrease in critical conductivity associated with a given mass flux of hydrogen is

$$\Delta k_c = \frac{\pi G \rho_0^2 L_p^4 \alpha_H}{6\gamma^2 M_C T_C} \left(\frac{f_\gamma \left(\frac{R_C}{L_p} \right)}{f_k \left(\frac{R_C}{L_p} \right)} \right) \left(\frac{dM_H}{dt} \right)_{wm}, \quad (18)$$

which implies $\Delta k_c = -20$ W/m/K × (2700 K / T_C) × [(dM_H/dt)$_{wm}$ / 1431 kg/s]. Critically, the mass flux of hydrogen across the CMB (Equation 5) decreases quicker than the upper limit from Equation 17, which is consistent with a dynamo existing at early times but not after a critical balance between Q_C and Q_H was reached. If $C_{H,LM} = 4 \times 10^{-4}$, then the average values of (dM_H/dt)$_{wm}$ at 500 Myr for $D_{H,BL} = 10^{-5}$, 10^{-6}, 10^{-7}, and 10^{-8} m^2/s are ~650, 420, 170, and 60 kg/s, respectively. These mass fluxes correspond to $-\Delta k_c = 9$, 6, 2, and 1 W/m/K. While seemingly small, these variations may translate to changes of ~100–750 Myr in the predicted lifetime of the dynamo. If the lower mantle initially contained roughly half the saturation value of water ($C_{H,LM} = 10^{-3}$), then $-\Delta k_c = 22$, 15, 6, and 2 W/m/K if $D_{H,BL} = 10^{-5}$, 10^{-6}, 10^{-7}, and 10^{-8} m^2/s, respectively. Critical values of >100 W/m/K in models with $T_C = 2900$ K and $\mu_R = 10^{22}$ Pa s are still unacceptably high. Ultimately, hydrogenation could allow super-adiabatic heat flow from the core to persist far beyond the Noachian.

4 Discussion

Any model of Martian history relies on simplifying assumptions. First, we assumed that hydrogen was efficiently transported in the basal mantle and partitioned into the core. Second, we assumed that the mantle always convected in the stagnant-lid regime without significant changes in mineralogy over time. Despite these limitations, the basic idea that hydrogenation alters the relative buoyancy of material on both sides of the CMB may have implications for the ongoing and planned exploration of Mars and other planets.

4.1 Behavior of hydrogen in the mantle and core

Experiments have not fully constrained the partitioning behavior of hydrogen. Shibazaki et al. (2009) inferred $D^H_{Fe/Rw} \sim 26$ at ~19 GPa based on in-situ estimation of hydrogen abundances in metal after equilibration with solid ringwoodite (Shibazaki et al., 2009). A recent investigation inferred $D^H_{Fe/Rw} \sim 0.2$ at similar conditions based on measuring the abundance of hydrogen in metal after equilibration with liquid silicate and quench to ambient pressure (1 bar) (Clesi et al., 2018). However, this new study only placed a lower bound on $D^H_{Fe/Rw}$ because some unknown amount of hydrogen escaped during decompression since its solubility is only of order ~10 ppm in metal at low pressures. Moreover, the distinction between solid and liquid silicate is potentially important. If $D^H_{Fe/Rw}$ is relatively low for liquid silicates, then hydrogen would remain in the magma ocean during planetary differentiation but partition into the core at later times. More experiments are required to resolve these ambiguities and constrain the partition coefficient for hydrogen as functions of pressure, temperature, and sulfur content. Future studies should also tighten the uncertainty on the diffusivity of hydrogen in the Martian core below the current factor

of two. Finally, resolving the debate about the thermal conductivity of iron-rich cores is a priority for Mars and all terrestrial planets.

Modeling investigations should consider hydrogen as a likely constituent of the core, which may affect the dynamical regimes for an iron/sulfur core (Davies & Pommier, 2018). Hydrogen substitutes for sulfur as a light element to match geodetic and dynamical constraints (Gudkova & Zharkov, 2004), which is perhaps desirable given evidence that sulfur could be less abundant than typically assumed (Wang & Becker, 2017)—closer to the <5 wt% expected for Earth's core from cosmochemical and mineral physics constraints (Dreibus & Palme, 1996; Mahan et al., 2017; Suer et al., 2017). Hydrogen also depresses the solidus (Shibazaki et al., 2011), helping to explain why the core remains at least partially liquid today (Gudkova & Zharkov, 2004; Yoder et al., 2003). Two- or three-dimensional simulations should include chemical reactions at the CMB, which may produce iron-rich structures in the lower mantle. Spatially-resolved simulations could also investigate axisymmetric forcing from heterogeneous hydration states and temperatures of material near the CMB (Stanley et al., 2008). Ultimately, fully dynamical simulations are required to validate whether partial melting can increase the effective diffusivity of hydrogen in the basal mantle.

Downward entrainment of hydrogen in the core is a key avenue for future research. In general, a Richardson number governs the entrainment rate of stratification above a convective region (e.g., Landeau et al., 2016), although refinement of the relevant scaling law is desired. Moreover, double-diffusive instabilities in the core may mirror Earth's high-latitude oceans where cold, fresh water overlies warm, salt water (e.g., Huppert & Turner, 1981; Turner, 1973), since the stabilizing component (hydrogen) has slow diffusivity compared to heat. However, double-diffusive convection in spherical geometry with rotation and magnetic fields is complex and thus poorly understood (e.g., Bouffard et al., 2017; Dietrich & Wicht, 2018; Moll & Garaud, 2016). A critical question is whether double-diffusive layers speed downward transport as in simple, one-dimensional scalings (e.g., Leconte & Chabrier, 2012, 2013).

4.2 Plausibility of delayed hydrogenation

Modelers often assume equilibrium crystallization of the magma ocean after accretion so whole-mantle convection begins immediately after solidification (Breuer et al., 2016). In contrast, fractional crystallization of the magma ocean would produce a gravitationally unstable configuration that overturns in <100 Myr via Rayleigh-Taylor instability (Elkins-Tanton, 2008; Elkins-Tanton et al., 2003, 2005). Iron-rich cumulates blanketing the CMB after this overturn are compositionally dense but cold enough to facilitate sufficient cooling of the core to drive a dynamo at early times. Assuming ideal fractional crystallization, the basal cumulates are enriched in incompatible components such as potassium and water but remain stable against convection for the entire age of Mars (Breuer et al., 2016; Elkins-Tanton et al., 2005; Plesa & Breuer, 2014). Complications such as inefficient crystal/melt segregation and solid-state convection that mixes material below the solidification front tend to reduce the density gradient across the mantle and permit convective overturn of the lowermost mantle (Breuer et al., 2016; Scheinberg et al., 2014). Models with delayed mantle convection are potentially realistic compared to the end-member cases of either fractional or equilibrium crystallization. In this case, the onset of whole-mantle convection could correspond to the demise of the dynamo if the associated increase in the hydrogenation rate dominates the additional heat transport.

A bridgmanite-bearing layer in the lower mantle could also cause hydrogenation of the core to start slowly but then hasten. Recent studies show that the solubility of water in bridgmanite and ferropericlase is much lower than in ringwoodite at lower pressure (Bolfan-Casanova, 2005; Bolfan-Casanova et al., 2003). At early times, Mars may have hosted a bridgmanite-bearing layer if the radius of the core is ~1470–1600 km. Because of the negative Clapeyron slope of the post-spinel transition (Fei et al., 2004; Shim et al., 2001), any bridgmanite-bearing layer becomes progressively thinner with secular cooling—and eventually disappears—because of the transition to ringwoodite. A small core is consistent with the observed mass and moment of inertia of Mars (Bertka & Fei, 1997). However, recent studies argue that other geodetic constraints indicate that the radius of the core is >1700 km—militating against a bridgmanite-bearing layer ever existing (Khan et al., 2018; Plesa et al., 2018; Rivoldini et al., 2011). Of course, a bridgmanite-bearing layer and delayed convection in the lower mantle are not mutually exclusive. Invoking a delay before the hydrogenation of the core would become necessary if future work suggests that the effective diffusivity of hydrogen exceeds that required to match the observed lifetime of the dynamo assuming continuous whole-mantle convection.

4.3 Predictions for Mars and other planets

The NASA InSight mission and future geophysical observatories should better constrain these models. Simply measuring the radius of the core would indicate whether a bridgmanite-bearing layer may have existed and constrain the abundances of light elements in the core. Electromagnetic sounding could constrain the present-day hydration state of the lower mantle. The seismic wavespeed profile of the outer core would provide a proxy for compositional gradients, although detecting a stratified layer below the CMB would require extremely high-quality data (Helffrich, 2017). Models with alternative sources of stratification such as iron snow in a sulfur-rich core predict only ~100 km of stratification (Davies & Pommier, 2018) compared to >100 km from hydrogenation. Hydrogenation is the best explanation for any future detection of chemical stratification if the temperature at the CMB exceeds the iron/sulfur liquidus. Detecting an inner core would argue against a high primordial abundance of hydrogen in the core because hydrogen would lower the liquidus by several hundred degrees. An inner core would also increase the minimum mass flux of hydrogen required to suppress a dynamo by an amount that should be calculated in future studies. Exclusion of light elements from an inner core could otherwise drive convection in the well-mixed core even if the uppermost core is stably stratified (e.g., Christensen & Wicht, 2008; Labrosse, 2015; Nakagawa, 2018).

Understanding the short-lived Martian dynamo has implications for all terrestrial planets. The so-called E’ layer atop Earth’s core is probably enriched in light elements compared to the bulk fluid, but downward entrainment obviously has not suppressed our dynamo. The E’ layer likely formed from core merging following a giant impact (Landeau et al., 2016) or efficient equilibration across a liquid/liquid interface during the solidification of a basal magma ocean (Brodholt & Badro, 2017; Buffett & Seagle, 2010; Nakagawa, 2018). Either scenario would create steep compositional gradients that prevent double-diffusive processes and/or penetrative convection from entraining buoyant fluid into the well-mixed core. However, completely neglecting this energy sink is not necessarily justified. Sub-critical entrainment could buffer the increase in convective vigor provoked by increased core/mantle heat flow. Speculatively, this negative feedback might help explain why paleointensity measurements seem relatively constant over time (Aubert et al., 2009; Driscoll, 2016; Landeau et al., 2017; Smirnov et al., 2016).

Mercury has a relatively small volume ratio between the mantle and core, so its mantle can store relatively little water. Earth and Venus are too large for hydrous silicates such as ringwoodite and wadsleyite to contact the core after planetary accretion and differentiation (e.g., Bolfan-Casanova, 2005). Planetary size is critical to chemical processes that govern dynamos over geologic time. This trend could manifest in exoplanets (Driscoll, 2018)—small and large planets are perhaps more likely to host long-lived dynamos than mid-sized planets.

5 Conclusions

Mars-sized planets are unique because their lower mantles may store orders-of-magnitude more water than silicates that are stable at comparatively reduced and elevated pressures. Hydrogen from hydrated silicates such as ringwoodite is exchanged for iron from the core via redox reaction at the core/mantle boundary, so the bulk FeO content of the mantle gradually increases. We adapted parameterized models for the long-term evolution of Mars to quantify the rate at which the core is hydrogenated. Core temperatures exceed the mantle solidus for billions of years, so partial melting could speed hydrogen transport in the basal mantle with effective diffusivities far above the measured values of ~10^{-8}–10^{-7} m^2/s in solid silicates. Most of the water that the Martian mantle contained after planetary accretion could have been lost to the core—enough to form a global ocean with a depth >0.25–1 km on the surface. The depth of this "lost ocean" rises to ~7 km if the basal mantle was nearly water-saturated and the effective diffusivity of hydrogen was ~10^{-5} m^2/s. Rapid hydrogenation represents an energy sink that may invalidate the assumption that the core remains well-mixed and vigorously convective while the heat flow across the core/mantle boundary is super-adiabatic. Future work should determine whether injecting hydrogen into the top of the core may suppress convection in the underlying fluid, which is a complicated problem. Critically, hydrogenation of the core could have foreshortened the lifetime of the early dynamo and produced seismic signatures that await detection today.

Acknowledgments and Data

Three anonymous reviewers and the editor (S.A. Hauck) provided many constructive comments that improved the manuscript. We thank M. Bouffard, L. Elkins-Tanton, S. Desch, B. Ko, M. Li, and D. J. Stevenson for many helpful discussions. J.G.O'R. was supported by ASU's SESE Exploration Postdoctoral Fellowship. S.-H. Shim was supported by the Keck foundation, the NSF (EAR1321976), and NExSS/NASA (NNX15AD53G). Data sharing is not applicable to this article as no new data were created or analyzed in this study.

Constant	Definition	Value	Units	Source
Boundary layer in the mantle				
R_C	Radius of the core	1758	km	1
A_C	Surface area of the core	3.9×10^{13}	m^2	1
k_M	Thermal conductivity of the lower mantle	4	W/m/K	2
κ_M	Thermal diffusivity of the lower mantle	10^{-6}	m^2/s	2
g	Gravitational acceleration at the core/mantle boundary	3.27	m/s^2	1
ρ_M	Density of the lower mantle	3476	kg/m^3	2
α_M	Coefficient of thermal expansion in the lower mantle	2×10^{-5}	K^{-1}	2
Ra_{crit}	Critical Rayleigh number for the convective overturn	2000		2
E	Activation energy in the definition of mantle viscosity	300	kJ/mol	2
T_R	Reference temperature for mantle viscosity	1600	K	2
$D^H_{Fe/rw}$	Partition coefficient for hydrogen between liquid iron and solid ringwoodite (mass fractions)	9		3
$C_{W,UM}$	Average mass fraction of water in the upper mantle	2×10^{-4}		
T_U	Potential temperature of the mantle	1750	K	1
Radial structure and dynamo energetics in the core				
$D_{H,C}$	Diffusivity of hydrogen in the core	1.2×10^{-7}	m^2/s	4
f_H	Mass fraction of hydrogen in water	0.112		
ρ_C	Density of the uppermost core	6439	kg/m^3	1
α_T	Coefficient of thermal expansion in the core	10^{-5}	K^{-1}	1
α_H	Coefficient of compositional expansion for hydrogen	7.96		1
κ_T	Thermal diffusivity of the core	8.3×10^{-6}	m^2/s	1
Ω_M	Diurnal frequency of Mars	7.1×10^{-5}	Hz	
ρ_0	Central density in the density profile for the core	6997	kg/m^3	1
M_C	Total mass of the core	4.88×10^{23}	kg	1
C_p	Specific heat of the core	750	J/kg/K	2
L_p	Length scale in the density profile for the core	6413	km	1
A_p	Constant in density profile for the core	0.8104		1
K	Effective modulus in density profile	281.3	GPa	1
K'	Effective modulus derivative in density profile	4.221		1
γ	Average Grüneisen parameter in the core	1.376		1
Thermochemical evolution				
Δt	Length of each model timestep	1	Myr	1
$[K]_C$	Concentration of potassium in the core	80 *0–80*	ppm	2
k_C	Thermal conductivity of the core	53 *5–115*	W/m/K	2, 5
$C_{H,LM}$	Average mass fraction of hydrogen in the lower mantle	4×10^{-4} *$0.4–1 \times 10^{-3}$*		3
$D_{H,BL}$	Effective diffusivity of hydrogen in the boundary layer	10^{-6} *$10^{-5}–10^{-8}$*	m^2/s	3
μ_R	Reference viscosity in the boundary layer	10^{23} *$10^{22}–10^{24}$*	Pa s	2
$T_C(0)$	Initial temperature of the core at the CMB	2700 *2300–2900*	K	2

Table 1. Definitions of key constants. Nominal values used in the reference model are listed above the italicized ranges explored in sensitivity tests. Sources: 1) Sections 2.3 and 2.4, Supporting Information, and references therein; 2) Stevenson et al. (1983), Fraeman & Korenaga (2010), and references therein; 3) Shibazaki et al. (2009); 4) Depuydt and Parlee (1972), Posner et al. (2017), Umemoto and Hirose (2015); 5) Deng et al. (2013).

Variable	Definition	Units
Mantle		
t	Time after planetary differentiation and solidification of the mantle	s
Q_C	Total heat flow across the CMB	W
ΔT_{BL}	Temperature contrast across the boundary layer	K
T_L	Temperature of the lower mantle above the boundary layer	K
μ_{BL}	Average dynamic viscosity in the boundary layer	Pa s
$\mu_M(T)$	Dynamic viscosity of the mantle as a function of temperature	Pa s
δ_{BL}	Thickness of the thermal boundary layer	m
t_{ov}	Timescale for convective overturn of the boundary layer	s
h	Thickness of a chemical boundary layer	m
$\Delta C_{H,BL}$	Change in the mass fraction of hydrogen across the LMBL	
X^H_{Fe}	Mass fraction of hydrogen in the core	
X^H_{rw}	Mass fraction of hydrogen in ringwoodite	
$(\mathrm{d}M_H/\mathrm{d}t)_{cmb}$	Total mass flux of hydrogen across the CMB into the core	kg/s
$M_{PM}{}^H$	Mass of hydrogen in the primitive mantle	kg
$M_{SM}{}^H$	Mass of hydrogen in the source mantle	kg
$M_S{}^H$	Mass of hydrogen degassed to the surface/atmosphere	kg
$M_C{}^H$	Mass of hydrogen lost to the core	kg
ΔV_{proc}	Volume of mantle that undergoes partial melting to produce crust	m^3
Core		
Φ	Total dissipation available for a dynamo	W
Q_S	Total heat flow associated with secular cooling of the core	W
$\tilde{Q}_S$	Total heat flow associated with secular cooling divided by the cooling rate of the core	J/K
Q_R	Total radiogenic heating in the well-mixed core	W
Q_H	Total gravitational energy associated with mixing hydrogen into the well-mixed core	W
Q_{ad}	Total adiabatic heat flow in the well-mixed core	W
Q_{crit}	Minimum heat flow across the CMB required to sustain a dynamo	W
$\mathrm{d}T_C/\mathrm{d}t$	Cooling rate of the core	K/s
dC_H/dz	Change in the hydrogen mass fraction with depth in a stratified layer	m^{-1}
$C_{H,SL}$	Average mass fraction of hydrogen in the stratified layer	
h_{SL}	Thickness of the stratified layer	m
N_H	Buoyancy frequency associated with stratification in the core	s^{-1}
$(\mathrm{d}M_H/dt)_{wm}$	Total mass flux of hydrogen that convection tries to mix downwards	kg/s
Δk_c	Decrease in the critical conductivity associated with hydrogenation	W/m/K
E_K	Entropy sink associated with adiabatic conduction of heat	W/K
$T_a(r)$	Adiabatic temperature profile in the core	K
T_0	Temperature at the center of the core	K
T_D	Average temperature in the well-mixed core	K
T_S	Effective temperature of dissipation associated with secular cooling	K

Table 2. Definitions of key model outputs.

Figure 1. The Martian dynamo dissipates after the cooling rate of the core drops below the critical value required to sustain convection in the core. **(a)** The lower mantle can store much more water than the upper mantle above a depth of ~1000 km. The structure and dynamics of the lower mantle boundary layer (LMBL) determine the rate at which hydrated silicates are delivered to the core/mantle boundary (CMB) where hydrogen can partition into metal. The mantle becomes progressively iron-rich in exchange. At early times, the core convects vigorously. **(b)** After the cooling rate of the core becomes sub-critical, convection in the core ceases and the global magnetic field dissipates. Whether the critical heat flow is significantly larger than the conventional, adiabatic limit depends on whether double-diffusive processes and/or penetrative convection would tend to mix large amounts of hydrogen into the convective system. In any case, a stratified, hydrogen-rich layer grows from the top of the core to a thickness of >100 km at present day.

Figure 2. One representative model shows how mantle convection can deliver the majority of primordial water from the mantle to the core. **(a)** Potential temperature of the mantle (blue), average temperature of the core (orange), and temperatures at the upper (black) and lower (red) boundaries of the LMBL. **(b)** Total heat flow from the mantle to the lithosphere (black) and then the surface (blue). **(c)** Crustal thickness. **(d)** Average viscosity in the LMBL. **(e)** Timescale for convective overturn of the LMBL. **(f)** Partitioning of hydrogen between the mantle (black), core (red), and surface (blue). The core is considered a sink of water although the oxygen atoms remain in the mantle as FeO. Water delivered to the surface may be lost later to the atmosphere and space. **(g)** Total heat flow across the CMB (black) compared to the adiabatic heat flow (purple, dotted), partitioned between secular cooling (brown) and radiogenic heating (orange). **(h)** Total dissipation in the core available for a dynamo (black) including secular cooling (brown) and radiogenic heating (orange) as sources and thermal conduction (purple) as sinks. Here the hydrogen that crossed the CMB was assumed to remain in a thin, stratified layer at the top of the core that did not affect the energy and dissipation budgets in the well-mixed core. The thermal conductivity of the core was tuned so the total dissipation becomes negative after 500 Myr to match the lifetime of the Martian dynamo.

Figure 3. Our models reinforce the argument from Shibazaki et al. (2009) that an ocean-worth of water was transported from the mantle into the core, where a stratified layer may await detection today. **(a)** Predicted masses of hydrogen ingested by the core over time according to our model with $D_{H,BL} = 10^{-6}$, 10^{-7}, and 10^{-8} m^2/s (black lines), the scaling analyses from Shibazaki et al. (2009) (blue line), and our representative model re-ran with the parameterization of Ruedas et al. (2013) and $D_{H,BL} \sim 10^{-8.5}$ m^2/s according to their temperature-dependent expression derived from the experiments of Hae et al. (2006) (red line). **(b)** Stability of a stratified layer at the top of the core as a function of its hydrogen content and thickness. The buoyancy frequency was computed assuming a linear compositional gradient and ratioed to the rotational rate of Mars.

Figure 4. The core is an important sink of water even if hydrogenation does not dominate the dissipation budget for the dynamo. Here 192 models with $C_{H,LM} = 4 \times 10^{-4}$ **(a)** and 10^{-3} **(b)** illustrate the effects of varying initial values of three key parameters: $[K]_C$ (filled or empty symbol), T_C (symbol color), and μ_R (symbol shape). Blue shading shows the range of conductivity values that are expected for the Martian core based on previous experimental and modeling studies. For each model, the final abundance of hydrogen in the core was converted

into a mass of water, which is then scaled by the surface area of Mars to obtain an equivalent thickness for a global ocean. Critically, models with $D_{H,BL} \geq 10^{-8}$ m^2/s predict that the core ingested the equivalent of a global ocean with a thickness of ≥240 m.

Figure 5. Hydrogen is efficiently transported into the core if its effective diffusivity in the basal mantle is relatively high. The black lines are the critical mass fluxes above which there is not enough energy in the convecting system to mix hydrogen throughout the entire core. Either the dynamo-generating region would shrink or convection in the core would cease entirely. The solid black line is based on a nominal thermal conductivity for the core (k_C = 40 W/m/K) that implies an adiabatic heat flow of Q_{ad} ~ 0.5 TW. The dashed black lines are the dynamo limits if k_C is adjusted by ±20 W/m/K, which changes Q_{ad} by roughly ±0.25 TW. The red lines show the predicted hydrogenation rates calculated from Equations 1–6 for effective diffusivities of hydrogen in the LMBL of $D_{H,BL} = 10^{-5}$, 10^{-6}, and 10^{-7} m^2/s with lighter shades indicating lower diffusivities. Effective diffusivities >10^{-7} m^2/s probably require that partial melting near the CMB, which should occur in our models because T_C typically exceeds the mantle solidus, enhances hydrogen transport. These calculations assume T_L = 2025 K, $\mu_R = 10^{23}$ Pa s, and $C_{H,LM} = 4 \times 10^{-4}$ as at the start of our representative model.

References

Acuna, M. H., Connerney, J. E. P., Ness, N. F., Lin, R. P., Mitchell, D., Carlson, C. W., et al. (1999). Global Distribution of Crustal Magnetization Discovered by the Mars Global Surveyor MAG/ER Experiment. *Science*, *284*(5415), 790–793. https://doi.org/10.1126/science.284.5415.790

Aubert, J., Labrosse, S., & Poitou, C. (2009). Modelling the palaeo-evolution of the geodynamo. *Geophysical Journal International*, *179*(3), 1414–1428. https://doi.org/10.1111/j.1365-246X.2009.04361.x

Badro, J., Siebert, J., & Nimmo, F. (2016). An early geodynamo driven by exsolution of mantle components from Earth's core. *Nature*, *536*(7616), 326–328. https://doi.org/10.1038/nature18594

Bercovici, D., & Karato, S. (2003). Whole-mantle convection and the transition-zone water filter. *Nature*, *425*(6953), 39–44. https://doi.org/10.1038/nature01918

Bertka, C. M., & Fei, Y. (1997). Mineralogy of the Martian interior up to core-mantle boundary pressures. *Journal of Geophysical Research: Solid Earth*, *102*(B3), 5251–5264. https://doi.org/10.1029/96JB03270

Blanchard, I., Siebert, J., Borensztajn, S., & Badro, J. (2017). The solubility of heat-producing elements in Earth's core. *Geochemical Perspectives Letters*, 1–5. https://doi.org/10.7185/geochemlet.1737

Bolfan-Casanova, N. (2005). Water in the Earth's mantle. *Mineralogical Magazine*, *69*(3), 229–258. https://doi.org/10.1180/0026461056930248

Bolfan-Casanova, Nathalie, Keppler, H., & Rubie, D. C. (2003). Water partitioning at 660 km depth and evidence for very low water solubility in magnesium silicate perovskite. *Geophysical Research Letters*, *30*(17), n/a-n/a. https://doi.org/10.1029/2003GL017182

Bouffard, M., Labrosse, S., Choblet, G., Fournier, A., Aubert, J., & Tackley, P. J. (2017). A particle-in-cell method for studying double-diffusive convection in the liquid layers of planetary interiors. *Journal of Computational Physics*, *346*, 552–571. https://doi.org/10.1016/j.jcp.2017.06.028

Boyce, J. M., Mouginis-Mark, P., & Garbeil, H. (2005). Ancient oceans in the northern lowlands of Mars: Evidence from impact crater depth/diameter relationships. *Journal of Geophysical Research E: Planets*, *110*(3), 1–15. https://doi.org/10.1029/2004JE002328

Brennan, M. C., Fischer, R. A., & Irving, J. C. E. (2019). Core Formation and Geophysical Properties of Mars. *Journal of Geophysical Research: Planets*, in review. https://doi.org/10.31223/osf.io/j654b

Breuer, D., Plesa, A. C., Tosi, N., & Grott, M. (2016). Water in the Martian interior—The geodynamical perspective. *Meteoritics and Planetary Science*, *51*(11), 1959–1992.

https://doi.org/10.1111/maps.12727

Brodholt, J., & Badro, J. (2017). Composition of the low seismic velocity E' layer at the top of Earth's core. *Geophysical Research Letters*, *44*(16), 8303–8310. https://doi.org/10.1002/2017GL074261

Buffett, B. A., & Seagle, C. T. (2010). Stratification of the top of the core due to chemical interactions with the mantle. *Journal of Geophysical Research*, *115*(B4), B04407. https://doi.org/10.1029/2009JB006751

Caracas, R., & Panero, W. R. (2017). Hydrogen mobility in transition zone silicates. *Progress in Earth and Planetary Science*, *4*(1). https://doi.org/10.1186/s40645-017-0119-8

Chidester, B. A., Rahman, Z., Righter, K., & Campbell, A. J. (2017). Metal-silicate partitioning of U: Implications for the heat budget of the core and evidence for reduced U in the mantle. *Geochimica et Cosmochimica Acta*, *199*, 1–12. https://doi.org/10.1016/j.gca.2016.11.035

Christensen, U R. (2010). Dynamo Scaling Laws and Applications to the Planets. *Space Science Reviews*, *152*(1–4), 565–590. https://doi.org/10.1007/s11214-009-9553-2

Christensen, Ulrich R., & Wicht, J. (2008). Models of magnetic field generation in partly stable planetary cores: Applications to Mercury and Saturn. *Icarus*, *196*(1), 16–34. https://doi.org/10.1016/j.icarus.2008.02.013

Clesi, V., Bouhifd, M. A., Bolfan-Casanova, N., Manthilake, G., Schiavi, F., Raepsaet, C., et al. (2018). Low hydrogen contents in the cores of terrestrial planets. *Science Advances*, *4*(3), e1701876. https://doi.org/10.1126/sciadv.1701876

Connerney, J. E. P., Acuña, M. H., Ness, N. F., Spohn, T., & Schubert, G. (2004). Mars Crustal Magnetism. *Space Science Reviews*, *111*(1/2), 1–32. https://doi.org/10.1023/B:SPAC.0000032719.40094.1d

Davies, C. J., & Pommier, A. (2018). Iron snow in the Martian core? *Earth and Planetary Science Letters*, *481*, 189–200. https://doi.org/10.1016/j.epsl.2017.10.026

Davies, C. J., Pozzo, M., Gubbins, D., & Alfè, D. (2018). Partitioning of Oxygen Between Ferropericlase and Earth's Liquid Core. *Geophysical Research Letters*, *45*(12), 6042–6050. https://doi.org/10.1029/2018GL077758

Dehant, V., Lammer, H., Kulikov, Y. N., Grießmeier, J. M., Breuer, D., Verhoeven, O., et al. (2007). Planetary magnetic dynamo effect on atmospheric protection of early Earth and Mars. *Space Science Reviews*, *129*(1–3), 279–300. https://doi.org/10.1007/s11214-007-9163-9

Deng, L., Seagle, C., Fei, Y., & Shahar, A. (2013). High pressure and temperature electrical resistivity of iron and implications for planetary cores. *Geophysical Research Letters*, *40*(1), 33–37. https://doi.org/10.1029/2012GL054347

Depuydt, P. J., & Parlee, N. A. D. (1972). The diffusion of hydrogen in liquid iron alloys. *Metallurgical and Materials Transactions B*, *3*(2), 529–536. https://doi.org/10.1007/BF02642058

Dietrich, W., & Wicht, J. (2018). Penetrative Convection in Partly Stratified Rapidly Rotating Spherical Shells. *Frontiers in Earth Science*, *6*, 1–14. https://doi.org/10.3389/feart.2018.00189

Dreibus, G., & Palme, H. (1996). Cosmochemical constraints on the sulfur content in the Earth's core. *Geochimica et Cosmochimica Acta*, *60*(7), 1125–1130. https://doi.org/10.1016/0016-7037(96)00028-2

Driscoll, P., & Bercovici, D. (2013). Divergent evolution of Earth and Venus: Influence of degassing, tectonics, and magnetic fields. *Icarus*, *226*(2), 1447–1464. https://doi.org/10.1016/j.icarus.2013.07.025

Driscoll, P. E. (2016). Simulating 2 Ga of geodynamo history. *Geophysical Research Letters*, *43*(11), 5680–5687. https://doi.org/10.1002/2016GL068858

Driscoll, P. E. (2018). Planetary Interiors, Magnetic Fields, and Habitability. In H. J. Deeg & J. A. Belmonte (Eds.), *Handbook of Exoplanets* (pp. 1–18). Springer International Publishing. https://doi.org/10.1007/978-3-319-30648-3_76-1

Duncan, M. S., Schmerr, N. C., Bertka, C. M., & Fei, Y. (2018). Extending the Solidus for a Model Iron-Rich Martian Mantle Composition to 25 GPa. *Geophysical Research Letters*, *45*(19), 10,211-10,220. https://doi.org/10.1029/2018GL078182

Elkins-Tanton, L.T. (2008). Linked magma ocean solidification and atmospheric growth for Earth and Mars. *Earth and Planetary Science Letters*, *271*(1–4), 181–191. https://doi.org/10.1016/j.epsl.2008.03.062

Elkins-Tanton, Linda T., Parmentier, E. M., & Hess, P. C. (2003). Magma ocean fractional crystallization and cumulate overturn in terrestrial planets: Implication for Mars. *Meteoritics & Planetary Science*, *1771*(12), 1753–1771.

Elkins-Tanton, Linda T., Zaranek, S. E., Parmentier, E. M., & Hess, P. C. (2005). Early magnetic field and magmatic activity on Mars from magma ocean cumulate overturn. *Earth and Planetary Science Letters*, *236*(1–2), 1–12. https://doi.org/10.1016/j.epsl.2005.04.044

Fei, H., Yamazaki, D., Sakurai, M., Miyajima, N., Ohfuji, H., Katsura, T., & Yamamoto, T. (2017). A nearly water-saturated mantle transition zone inferred from mineral viscosity. *Science Advances*, *3*(6), e1603024. https://doi.org/10.1126/sciadv.1603024

Fei, Y., Van Orman, J., Li, J., van Westrenen, W., Sanloup, C., Minarik, W., et al. (2004). Experimentally determined postspinel transformation boundary in Mg2SiO4 using MgO as an internal pressure standard and its geophysical implications. *Journal of Geophysical Research: Solid Earth*, *109*(B2), 1–8. https://doi.org/10.1029/2003JB002562

Filiberto, J. (2017). Geochemistry of Martian basalts with constraints on magma genesis. *Chemical Geology*, *466*, 1–14. https://doi.org/10.1016/j.chemgeo.2017.06.009

Fischer, R. A., Nakajima, Y., Campbell, A. J., Frost, D. J., Harries, D., Langenhorst, F., et al. (2015). High pressure metal–silicate partitioning of Ni, Co, V, Cr, Si, and O. *Geochimica et Cosmochimica Acta*, *167*, 177–194. https://doi.org/10.1016/j.gca.2015.06.026

Fraeman, A. A., & Korenaga, J. (2010). The influence of mantle melting on the evolution of Mars. *Icarus*, *210*(1), 43–57. https://doi.org/10.1016/j.icarus.2010.06.030

Gubbins, D., & Davies, C. J. (2013). The stratified layer at the core–mantle boundary caused by barodiffusion of oxygen, sulphur and silicon. *Physics of the Earth and Planetary Interiors*, *215*, 21–28. https://doi.org/10.1016/j.pepi.2012.11.001

Gudkova, T. V., & Zharkov, V. N. (2004). Mars: Interior structure and excitation of free oscillations. *Physics of the Earth and Planetary Interiors*, *142*(1–2), 1–22. https://doi.org/10.1016/j.pepi.2003.10.004

Hae, R., Ohtani, E., Kubo, T., Koyama, T., & Utada, H. (2006). Hydrogen diffusivity in wadsleyite and water distribution in the mantle transition zone. *Earth and Planetary Science Letters*, *243*(1–2), 141–148. https://doi.org/10.1016/j.epsl.2005.12.035

Helffrich, G. (2017). Mars core structure—concise review and anticipated insights from InSight. *Progress in Earth and Planetary Science*, *4*(1), 24. https://doi.org/10.1186/s40645-017-0139-4

Hirose, K., Morard, G., Sinmyo, R., Umemoto, K., Hernlund, J., Helffrich, G., & Labrosse, S. (2017). Crystallization of silicon dioxide and compositional evolution of the Earth's core. *Nature*, *543*(7643), 99–102. https://doi.org/10.1038/nature21367

Huppert, H., & Turner, J. (1981). Double-diffusive convection. *Journal of Fluid Mechanics*, *106*, 299–329. Retrieved from http://journals.cambridge.org/abstract_S0022112081001614

Jakosky, B. M., Grebowsky, J. M., Luhmann, J. G., Connerney, J., Eparvier, F., Ergun, R., et al. (2015). MAVEN observations of the response of Mars to an interplanetary coronal mass ejection. *Science*, *350*(6261), aad0210. https://doi.org/10.1126/science.aad0210

Jakosky, B. M., Slipski, M., Benna, M., Mahaffy, P., Elrod, M., Yelle, R., et al. (2017). Mars' atmospheric history derived from upper-atmosphere measurements of 38 Ar/ 36 Ar. *Science*, *355*(6332), 1408–1410. https://doi.org/10.1126/science.aai7721

Ke, Y., & Solomatov, V. S. (2009). Coupled core-mantle thermal evolution of early Mars. *Journal of Geophysical Research E: Planets*, *114*(7), 1–12. https://doi.org/10.1029/2008JE003291

Khan, A., Liebske, C., Rozel, A., Rivoldini, A., Nimmo, F., Connolly, J. A. D., et al. (2018). A Geophysical Perspective on the Bulk Composition of Mars. *Journal of Geophysical Research: Planets*, *123*(2), 575–611. https://doi.org/10.1002/2017JE005371

Kiefer, W. S., & Li, Q. (2016). Water undersaturated mantle plume volcanism on present-day Mars. *Meteoritics and Planetary Science*, *51*(11), 1993–2010. https://doi.org/10.1111/maps.12720

Korenaga, J. (2009). Scaling of stagnant-lid convection with Arrhenius rheology and the effects of mantle melting. *Geophysical Journal International*, *179*(1), 154–170. https://doi.org/10.1111/j.1365-246X.2009.04272.x

Labrosse, S. (2015). Thermal evolution of the core with a high thermal conductivity. *Physics of the Earth and Planetary Interiors*, *247*, 36–55. https://doi.org/10.1016/j.pepi.2015.02.002

Landeau, M., Olson, P., Deguen, R., & Hirsh, B. H. (2016). Core merging and stratification following giant impact. *Nature Geoscience*, *1*(September), 1–5. https://doi.org/10.1038/ngeo2808

Landeau, M., Aubert, J., & Olson, P. (2017). The signature of inner-core nucleation on the geodynamo. *Earth and Planetary Science Letters*, *465*, 193–204. https://doi.org/10.1016/j.epsl.2017.02.004

Lay, T., Hernlund, J., & Buffett, B. A. (2008). Core–mantle boundary heat flow. *Nature Geoscience*, *1*(1), 25–32. https://doi.org/10.1038/ngeo.2007.44

Leconte, J., & Chabrier, G. (2012). A new vision of giant planet interiors: Impact of double diffusive convection. *Astronomy & Astrophysics*, *540*, A20. https://doi.org/10.1051/0004-6361/201117595

Leconte, J., & Chabrier, G. (2013). Layered convection as the origin of Saturn's luminosity anomaly. *Nature Geoscience*, *6*(5), 347–350. https://doi.org/10.1038/ngeo1791

Li, Q., & Kiefer, W. S. (2007). Mantle convection and magma production on present-day Mars: Effects of temperature-dependent rheology. *Geophysical Research Letters*, *34*(16), 1–5. https://doi.org/10.1029/2007GL030544

Lillis, R. J., Robbins, S., Manga, M., Halekas, J. S., & Frey, H. V. (2013). Time history of the Martian dynamo from crater magnetic field analysis. *Journal of Geophysical Research: Planets*, *118*(7), 1488–1511. https://doi.org/10.1002/jgre.20105

Litasov, K. D., & Ohtani, E. (2007). Effect of water on the phase relations in Earth's mantle and deep water cycle. In E. Ohtani (Ed.), *Special Paper 421: Advances in High-Pressure Mineralogy* (pp. 115–156). Geological Society of America. https://doi.org/10.1130/2007.2421(08)

Mahan, B., Siebert, J., Pringle, E. A., & Moynier, F. (2017). Elemental partitioning and isotopic fractionation of Zn between metal and silicate and geochemical estimation of the S content of the Earth's core. *Geochimica et Cosmochimica Acta*, *196*, 252–270. https://doi.org/10.1016/j.gca.2016.09.013

Médard, E., & Grove, T. L. (2006). Early hydrous melting and degassing of the Martian interior.

Journal of Geophysical Research E: Planets, *111*(11), 1–15. https://doi.org/10.1029/2006JE002742

Moll, R., & Garaud, P. (2016). The Effect of Rotation on Oscillatory Double-Diffusive Convection (Semiconvection). *The Astrophysical Journal*, *834*(1), 44. https://doi.org/10.3847/1538-4357/834/1/44

Moore, K. M., & Bloxham, J. (2017). The construction of sparse models of Mars's crustal magnetic field. *Journal of Geophysical Research: Planets*, *122*(7), 1443–1457. https://doi.org/10.1002/2016JE005238

Nakagawa, T. (2018). On the thermo-chemical origin of the stratified region at the top of the Earth's core. *Physics of the Earth and Planetary Interiors*, *276*, 172–181. https://doi.org/10.1016/j.pepi.2017.05.011

Nakagawa, T., & Tackley, P. J. (2010). Influence of initial CMB temperature and other parameters on the thermal evolution of Earth's core resulting from thermochemical spherical mantle convection. *Geochemistry Geophysics Geosystems*, *11*(6). https://doi.org/10.1029/2010GC003031

Nakagawa, T., & Tackley, P. J. (2014). Influence of combined primordial layering and recycled MORB on the coupled thermal evolution of Earth's mantle and core. *Geochemistry Geophysics Geosystems*, *15*, 619–633. https://doi.org/10.1002/2013GC005128

O'Rourke, J. G., & Stevenson, D. J. (2016). Powering Earth's dynamo with magnesium precipitation from the core. *Nature*, *529*(7586), 387–389. https://doi.org/10.1038/nature16495

O'Rourke, J. G., Korenaga, J., & Stevenson, D. J. (2017). Thermal evolution of Earth with magnesium precipitation in the core. *Earth and Planetary Science Letters*, *458*, 263–272. https://doi.org/10.1016/j.epsl.2016.10.057

O'Rourke, J. G., Gillmann, C., & Tackley, P. (2018). Prospects for an ancient dynamo and modern crustal remanent magnetism on Venus. *Earth and Planetary Science Letters*, *502*, 46–56. https://doi.org/10.1016/j.epsl.2018.08.055

Pearson, D. G., Brenker, F. E., Nestola, F., McNeill, J., Nasdala, L., Hutchison, M. T., et al. (2014). Hydrous mantle transition zone indicated by ringwoodite included within diamond. *Nature*, *507*(7491), 221–224. https://doi.org/10.1038/nature13080

Phillips, R. J., Putzig, N. E., Egan, A. F., Zuber, M. T., Smrekar, S. E., Milkovich, S. M., et al. (2008). Mars north polar deposits: stratigraphy, age, and geodynamical response. *Science*, *320*(5880), 1182–1185. https://doi.org/10.1126/science.1157546

Plesa, A.-C., & Breuer, D. (2014). Partial melting in one-plate planets: Implications for thermo-chemical and atmospheric evolution. *Planetary and Space Science*, *98*, 55–65. https://doi.org/10.1016/j.pss.2013.10.007

Plesa, A.-C., Tosi, N., Grott, M., & Breuer, D. (2015). Thermal evolution and Urey ratio of Mars. *Journal of Geophysical Research: Planets*, *120*(5), 995–1010. https://doi.org/10.1002/2014JE004748

Plesa, A.-C., Padovan, S., Tosi, N., Breuer, D., Grott, M., Wieczorek, M. A., et al. (2018). The Thermal State and Interior Structure of Mars. *Geophysical Research Letters*, *45*(22), 12,198-12,209. https://doi.org/10.1029/2018GL080728

Pommier, A., Grove, T. L., & Charlier, B. (2012). Water storage and early hydrous melting of the Martian mantle. *Earth and Planetary Science Letters*, *333–334*, 272–281. https://doi.org/10.1016/j.epsl.2012.03.030

Posner, E. S., Rubie, D. C., Frost, D. J., & Steinle-Neumann, G. (2017). Experimental determination of oxygen diffusion in liquid iron at high pressure. *Earth and Planetary Science Letters*, *464*, 116–123. https://doi.org/10.1016/j.epsl.2017.02.020

Rivoldini, A., Van Hoolst, T., Verhoeven, O., Mocquet, A., & Dehant, V. (2011). Geodesy constraints on the interior structure and composition of Mars. *Icarus*, *213*(2), 451–472. https://doi.org/10.1016/j.icarus.2011.03.024

Roberts, J. H., Lillis, R. J., & Manga, M. (2009). Giant impacts on early mars and the cessation of the martian dynamo. *Journal of Geophysical Research E: Planets*, *114*(4), 1–10. https://doi.org/10.1029/2008JE003287

Ruedas, T., Tackley, P. J., & Solomon, S. C. (2013). Thermal and compositional evolution of the martian mantle: Effects of water. *Physics of the Earth and Planetary Interiors*, *220*, 50–72. https://doi.org/10.1016/j.pepi.2013.04.006

Sakamaki, K., Takahashi, E., Nakajima, Y., Nishihara, Y., Funakoshi, K., Suzuki, T., & Fukai, Y. (2009). Melting phase relation of FeHx up to 20 GPa: Implication for the temperature of the Earth's core. *Physics of the Earth and Planetary Interiors*, *174*(1–4), 192–201. https://doi.org/10.1016/j.pepi.2008.05.017

Sakamaki, T. (2017). Density of hydrous magma. *Chemical Geology*, *475*(November), 135–139. https://doi.org/10.1016/j.chemgeo.2017.11.012

Sakamaki, T., Suzuki, A., & Ohtani, E. (2006). Stability of hydrous melt at the base of the Earth's upper mantle. *Nature*, *439*(7073), 192–194. https://doi.org/10.1038/nature04352

Sandu, C., & Kiefer, W. S. (2012). Degassing history of Mars and the lifespan of its magnetic dynamo. *Geophysical Research Letters*, *39*(3), 3–7. https://doi.org/10.1029/2011GL050225

Scheinberg, A., Elkins-Tanton, L. T., & Zhong, S. J. (2014). Timescale and morphology of Martian mantle overturn immediately following magma ocean solidification. *Journal of Geophysical Research E: Planets*, *119*(3), 454–467. https://doi.org/10.1002/2013JE004496

Shibazaki, Y., Ohtani, E., Terasaki, H., Suzuki, A., & Funakoshi, K. ichi. (2009). Hydrogen partitioning between iron and ringwoodite: Implications for water transport into the Martian

core. *Earth and Planetary Science Letters*, *287*(3–4), 463–470. https://doi.org/10.1016/j.epsl.2009.08.034

Shibazaki, Y., Ohtani, E., Terasaki, H., Tateyama, R., Sakamaki, T., Tsuchiya, T., & Funakoshi, K. ichi. (2011). Effect of hydrogen on the melting temperature of FeS at high pressure: Implications for the core of Ganymede. *Earth and Planetary Science Letters*, *301*(1–2), 153–158. https://doi.org/10.1016/j.epsl.2010.10.033

Shim, S., Duffy, T. S., & Shen, G. (2001). The post-spinel transformation in Mg2SiO4 and its relation to the 660-km seismic discontinuity. *Nature*, *411*(6837), 571–574. https://doi.org/10.1038/35079053

Smirnov, A. V., Tarduno, J. A., Kulakov, E. V., McEnroe, S. A., & Bono, R. K. (2016). Palaeointensity, core thermal conductivity and the unknown age of the inner core. *Geophysical Journal International*, *205*(2), 1190–1195. https://doi.org/10.1093/gji/ggw080

Smrekar, S. E., Lognonné, P., Spohn, T., Banerdt, W. B., Breuer, D., Christensen, U., et al. (2019). *Pre-mission InSights on the Interior of Mars*. *Space Science Reviews* (Vol. 215). Springer Nature B.V. https://doi.org/10.1007/s11214-018-0563-9

Stanley, S., Elkins-Tanton, L., Zuber, M. T., & Parmentier, E. M. (2008). Mars' Paleomagnetic Field as the Result of a Single-Hemisphere Dynamo. *Science*, *321*(5897), 1822–1825. https://doi.org/10.1126/science.1161119

Stelzer, Z., & Jackson, A. (2013). Extracting scaling laws from numerical dynamo models. *Geophysical Journal International*, *193*(3), 1265–1276. https://doi.org/10.1093/gji/ggt083

Stevenson, D. J. (2001). Mars' core and magnetism. *Nature*, *412*(6843), 214–219. https://doi.org/10.1038/35084155

Stevenson, D. J. (2003). Planetary magnetic fields. *Earth and Planetary Science Letters*, *208*(1–2), 1–11. https://doi.org/10.1016/S0012-821X(02)01126-3

Stevenson, D. J. (2010). Planetary magnetic fields: Achievements and prospects. *Space Science Reviews*, *152*(1–4), 651–664. https://doi.org/10.1007/s11214-009-9572-z

Stevenson, D. J., Spohn, T., & Schubert, G. (1983). Magnetism and thermal evolution of the terrestrial planets. *Icarus*, *54*(3), 466–489. https://doi.org/10.1016/0019-1035(83)90241-5

Suer, T.-A., Siebert, J., Remusat, L., Menguy, N., & Fiquet, G. (2017). A sulfur-poor terrestrial core inferred from metal–silicate partitioning experiments. *Earth and Planetary Science Letters*, *469*, 84–97. https://doi.org/10.1016/j.epsl.2017.04.016

Sun, W., Yoshino, T., Sakamoto, N., & Yurimoto, H. (2015). Hydrogen self-diffusivity in single crystal ringwoodite: Implications for water content and distribution in the mantle transition zone. *Geophysical Research Letters*, *42*(16), 6582–6589. https://doi.org/10.1002/2015GL064486

Taylor, G. J. (2013). The bulk composition of Mars. *Chemie Der Erde - Geochemistry*, *73*(4), 401–420. https://doi.org/10.1016/j.chemer.2013.09.006

Turcotte, D. L., & Schubert, G. (2002). *Geodynamics*. New York: Cambridge University Press.

Turner, J. S. (1973). *Buoyancy Effects in Fluids*. Cambridge: Cambridge University Press. https://doi.org/10.1017/CBO9780511608827

Umemoto, K., & Hirose, K. (2015). Liquid iron-hydrogen alloys at outer core conditions by first-principles calculations. *Geophysical Research Letters*, *42*(18), 7513–7520. https://doi.org/10.1002/2015GL065899

Wade, J., Dyck, B., Palin, R. M., Moore, J. D. P., & Smye, A. J. (2017). The divergent fates of primitive hydrospheric water on Earth and Mars. *Nature*, *552*(7685), 391–394. https://doi.org/10.1038/nature25031

Wang, Z., & Becker, H. (2017). Chalcophile elements in Martian meteorites indicate low sulfur content in the Martian interior and a volatile element-depleted late veneer. *Earth and Planetary Science Letters*, *463*, 56–68. https://doi.org/10.1016/j.epsl.2017.01.023

Weiss, B. P., Vali, H., Baudenbacher, F. J., Kirschvink, J. L., Stewart, S. T., & Shuster, D. L. (2002). Records of an ancient Martian magnetic field in ALH84001. *Earth and Planetary Science Letters*, *201*(3–4), 449–463. https://doi.org/10.1016/S0012-821X(02)00728-8

Wenzel, M. J., Manga, M., & Jellinek, A. M. (2004). Tharsis as a consequence of Mars' dichotomy and layered mantle. *Geophysical Research Letters*, *31*(4), 3–7. https://doi.org/10.1029/2003GL019306

Wieczorek, M. A., & Zuber, M. T. (2004). Thickness of the Martian crust: Improved constraints from geoid-to-topography ratios. *Journal of Geophysical Research*, *109*(E1), E01009. https://doi.org/10.1029/2003JE002153

Williams, J.-P., & Nimmo, F. (2004). Thermal evolution of the Martian core: Implications for an early dynamo. *Geology*, *32*(2), 97. https://doi.org/10.1130/G19975.1

Yoder, C. F., Konopliv, A. S., Yuan, D. N., Standish, E. M., & Folkner, W. M. (2003). Fluid core size of Mars from detection of the solar tide. *Science*, *300*(5617), 299–303. https://doi.org/10.1126/science.1079645

Journal of Geophysical Research: Planets

Supporting Information for

Hydrogenation of the Martian Core by Hydrated Mantle Minerals with Implications for the Early Dynamo

J. G. O'Rourke and S.-H. Shim

School of Earth and Space Exploration, Arizona State University, Tempe, AZ 85287

Contents of this file

Introduction

Text S1 explains our procedure for calculating the radial structure of the core of Mars. We also describe our equations of state for iron alloys with hydrogen and sulfur. Table S2 discusses the terms in our energetic model for the dynamo that were not defined in the main text. Figure S1 plots the diffusivity of hydrogen at relevant temperatures in solid silicates according to recent studies. Figure S2 shows our fiducial structure for the core. Table S1 gives the parameters in our equations of state. Table S2 gives the detailed output for all models shown in Figures 4.

Text S1.

S1.1 Thermoelastic properties of the core

We assume that the core is a ternary alloy composed only of Fe, S, and H. First, we compute the thermoelastic properties of three individual components: liquid Fe, Fe-10 wt% S (written as FeS10), and FeH. Here we assume that liquid Fe is a sufficient proxy for an Fe/Ni alloy. We consider isothermal compression and then isobaric heating to conditions (P, T) from a reference state (P_0, T_0). We use a third-order, Birch-Murnaghan equation-of-state (Khan et al., 2018):

$$P = -3\,\epsilon\,(1-2\epsilon)^{\frac{5}{2}}\left[K_{T,0} - \frac{3}{2}K_{T,0}\left(K'_{T,0} - 4\right)\epsilon\right], \quad (19)$$

$$\mathrm{K_T} = \frac{(1-2\epsilon)^{\frac{5}{2}}}{1 + (\mathrm{T}-\mathrm{T_0})\alpha(\mathrm{P})\mathrm{K'_{T,0}}\beta^{1.4}}\left[\mathrm{K_{T,0}} - \mathrm{K_{T,0}}\left(3\mathrm{K'_{T,0}} - 5\right)\epsilon + \frac{27}{2}\mathrm{K_{T,0}}\left(\mathrm{K'_{T,0}} - 4\right)\epsilon^2\right], \quad (20)$$

$$K'_T = K'_{T,0} + \left[3K'^2_{T,0} - 21K'_{T,0} + \frac{143}{3}\right], \quad (21)$$

where $\epsilon = 0.5(1-\beta^{-2/3})$ is Eulerian strain with $\beta = V(P)/V_0$. Here $V(P)$ is the molar volume at (P, T_0). The isothermal bulk modulus and its pressure derivative at T_0 are represented by $K_{T,0}$, and $K'_{T,0}$, respectively. The coefficient of thermal expansion changes with pressure as (Khan et al., 2018)

$$\alpha(P) = \alpha_0\, e^{-\frac{K'_{T,0}}{1.4}\left(1-\beta^{1.4}\right)}. \quad (22)$$

We compute $P(V)$ for a range of V sufficient to span conditions in the core. Then we interpolate to find $V(P)$. Finally, we calculate the volumetric expansion during heating from T_0 to T as

$$V(P,T) = V(P)e^{\alpha(P)(T-T_0)}. \quad (23)$$

Table S1 contains the parameters used in the equation-of-state for each component. We compute the bulk properties of the core by assuming ideal mixing of all three components. From mass balance, we calculate the mole fraction of each component as

$$X_{FeH} = \frac{w_H}{u_H}\left(\frac{M_{Fe}M_S}{M_SM_H + M_S(M_{Fe}-M_H)w_H + M_H(M_{Fe}-M_S)w_S}\right), \quad (24)$$

$$X_{FeS_{10}} = \frac{w_S}{u_S}\left(\frac{M_{Fe} - X_{FeH} f_H (M_{Fe} - M_H)}{M_S + (M_{Fe} - M_S) w_S}\right), \quad (25)$$

and $X_{Fe} = 1 - X_{FeS10} - X_{FeH}$. Here w_S and w_H are the weight fractions of sulfur and hydrogen in the core, respectively, with corresponding mole fractions X_S and X_H. The mole fractions of S in FeS_{10} and H in FeH are $u_S = 0.16214$ and $u_H = 0.5$, respectively. Constants M_{Fe}, M_S, and M_H are the atomic weights of each element. The molar volume of the solution is

$$V = \sum_{i=1}^{3} X_i V_i, \quad (26)$$

Likewise, we derive the bulk thermal expansion, the isothermal bulk modulus, and its derivative with respect to pressure as

$$\alpha = \frac{1}{V}\sum_{i=1}^{3} X_i \alpha_i V_i, \quad (27)$$

$$\frac{1}{K_T} = \frac{1}{V}\sum_{i=1}^{3} \frac{X_i V_i}{K_{T,i}}, \quad (28)$$

$$K_T' = -1 + \frac{K_T}{V}\sum_{i=1}^{3} \frac{X_i V_i}{K_{T,i}}\left(1 + K_{T,i}'\right). \quad (29)$$

We compute the Grüneisen parameter using an approximate relation (Khan et al., 2018):

$$\gamma = \frac{\frac{1}{2}K_T' - \frac{5}{6} + \frac{2}{9}PK_T^{-1}}{1 - \frac{4}{3}PK_T^{-1}}, \quad (30)$$

which we use alongside the adiabatic bulk modulus $K_S = K_T(1 + \alpha\gamma T)$ to calculate the adiabatic temperature gradient in the core. We also characterize the liquidus for the bulk alloy as

$$T_m(P, X_S, X_H) = T_{m,Fe}(P) - \left(\frac{T_{m,Fe}(P) - T_{S,e}(P)}{X_{S,e}(P)}\right) X_S - \Delta T_H X_H, \quad (31)$$

where $T_{m,\,Fe}$ is the melting temperature of pure Fe liquid. The eutectic temperature and sulfur concentration in the Fe-S system are $T_{S,e}$ and $X_{S,e}$, respectively (Rivoldini et al., 2011). We assume that $\Delta T_H = 1500$ K so stoichiometric FeH has a melting temperature

750 K below that of pure Fe at any pressure (Sakamaki et al., 2009; Shibazaki et al., 2009).

S1.2 Radial structure of the core

We construct a fiducial model for the structure of the core assuming spherical symmetry. Rather than self-consistently model the entire planet to match geodetic constraints like moment of inertia, we simply fix the central pressure and mass of the core and accept one model that produce pressures at the core/mantle boundary resembling results from more comprehensive studies (Khan et al., 2018; Rivoldini et al., 2011). If we take $m(r)$ as the total mass enclosed within a radius r, then assuming hydrostatic equilibrium yields

$$\frac{\partial P}{\partial r} = -\frac{Gm(r)\rho(P,T)}{r^2}. \tag{32}$$

We integrate this equation in combination with two others that describe conservation of mass,

$$\frac{\partial m}{\partial r} = 4\pi r^2 \rho(r). \tag{33}$$

and the adiabatic thermal gradient:

$$\frac{\partial T}{\partial r} = -\frac{T(r)\gamma(P,T)}{K_S(P,T)}\left(\frac{Gm(r)\rho(P,T)}{r^2}\right). \tag{34}$$

Figure S2 shows the radial profiles of pressure, density, temperature, and gravity that we derived in our fiducial model of the core as discussed in the main text.

Text S2.

Here we list the parameters in the energetic model for the dynamo that were not explicitly defined in the main text but are taken from Labrosse (2015) without modification. First, we used a useful function

$$f_c(x,\delta) = x^3\left[1 - \frac{3}{5}(\delta+1)x^2 - \frac{3}{14}(\delta+1)\big(2A_p - \delta\big)x^4\right]. \tag{35}$$

Next, the contribution to the energy budget from radiogenic heating is

$$Q_R = \frac{4}{3}\pi\rho_0 L_p^3 f_c\left(\frac{R_C}{L_p}, 0\right)\Lambda_C, \tag{36}$$

where Λ_C is the heating rate per unit mass, which is proportional to $[K]_C$. For example, if $[K]_C$ = 80 ppm, then $\Lambda_C \sim 3.35 \times 10^{-12}$ W/kg initially and $\sim 2.77 \times 10^{-13}$ W/kg after 4.5 Gyr. The average temperature of the core is

$$T_D = T_0\left[\frac{f_c\left(\frac{R_C}{L_p}, 0\right)}{f_c\left(\frac{R_C}{L_p}, -\gamma\right)}\right]. \tag{37}$$

Likewise, the effective temperature for dissipation associated with secular cooling is

$$T_S = T_0\left[\frac{f_c\left(\frac{R_C}{L_p}, \gamma\right)}{f_c\left(\frac{R_C}{L_p}, 0\right)}\right]. \tag{38}$$

Finally, the entropy sink associated with thermal conduction is

$$E_K = 16\pi\gamma^2 k_C L_p f_k\left(\frac{R_C}{L_p}\right), \tag{39}$$

which uses another useful function:

$$f_k(x) = 0.2x^5 + \left[1 + \frac{5}{7}\big(2 + 4A_p\big)x^2 + \frac{5}{9}\big(3 + 10A_p + 4A_p^2\big)x^4\right]. \tag{40}$$

Component	T_0 (K)	V (cm^3 mol^{-1})	α_0 ($10^{-5}K^{-1}$)	$K_{T,0}$ (GPa)	$K'_{T,0}$
Fe	1811	7.96	9.2	85.3	5.9
FeS_{10}	1923	9.45	10.0	63.0	4.8
FeH	1000	8.28	14.0	173.0	5.8

Table S1. Thermoelastic properties for three components of the core. Constants for components Fe and FeS_{10} were taken directly from a previous study (Khan et al., 2018) and references therein. Parameters for FeH were derived by fitting our equation-of-state to $V(P,T)$ predicted from a series of experiments (Sakamaki et al., 2009) over the ranges P = 10 to 50 GPa and T = 1000 to 2900 K.

Model input				Model output					
				$C_{H,LM} = 4 \times 10^{-4}$			$C_{H,LM} = 10^{-3}$		
$D_{H,BL}$ (m^2/s)	$[K]_C$ (ppm)	T_C (K)	$\log_{10}(\mu_R$ [Pa s])	k_c (W/m/K)	Δh_w (km)	$(dM_H/dt)_{cmb}$ (kg/s)	k_c (W/m/K)	Δh_w (km)	$(dM_H/dt)_{cmb}$ (kg/s)
-5	0	2300	22	14	2.97	609	14.1	7.17	1487
-5	0	2300	23	10.1	2.94	574	10.2	7.11	1400
-5	0	2300	24	6.7	2.94	575	6.7	7.1	1401
-5	0	2500	22	37.6	3.06	802	37.5	7.38	1954
-5	0	2500	23	23	2.98	568	22.9	7.23	1393
-5	0	2500	24	12.3	2.92	573	12.2	7.08	1398
-5	0	2700	22	67.6	3.08	805	67.6	7.42	1961
-5	0	2700	23	44.4	2.98	641	44.4	7.27	1583
-5	0	2700	24	24.9	2.9	568	24.9	7.06	1393
-5	0	2900	22	97.8	3.09	716	97.9	7.44	1755
-5	0	2900	23	68.5	2.98	723	68.5	7.28	1801
-5	0	2900	24	40.4	2.89	560	40.4	7.07	1384
-5	80	2300	22	28.2	3.09	719	28.3	7.43	1753
-5	80	2300	23	20	3.01	573	20.1	7.27	1399
-5	80	2300	24	12.9	2.93	575	13	7.09	1400
-5	80	2500	22	48.9	3.09	854	48.9	7.44	2077
-5	80	2500	23	31.2	3.01	567	31.3	7.3	1392
-5	80	2500	24	19.7	2.93	572	19.8	7.09	1397
-5	80	2700	22	80.8	3.09	829	80.9	7.44	2017
-5	80	2700	23	52.7	3	686	52.6	7.31	1696
-5	80	2700	24	29.8	2.93	567	29.8	7.12	1391
-5	80	2900	22	112.2	3.1	723	112.3	7.46	1774
-5	80	2900	23	78.1	2.98	755	78.1	7.3	1881
-5	80	2900	24	46	2.92	559	46	7.14	1382
-6	0	2300	22	13.8	1.86	362	13.7	4.76	935
-6	0	2300	23	10.2	1.78	333	10.3	4.54	858
-6	0	2300	24	6.7	1.75	333	6.7	4.46	859
-6	0	2500	22	39.4	2.18	518	39.5	5.58	1341
-6	0	2500	23	24.1	1.91	331	24.2	4.9	856
-6	0	2500	24	12.9	1.74	332	12.9	4.45	857
-6	0	2700	22	68.5	2.27	606	68.6	5.88	1579
-6	0	2700	23	45.4	1.99	376	45.4	5.16	979
-6	0	2700	24	25.5	1.72	331	25.5	4.43	855
-6	0	2900	22	97.8	2.28	634	98	5.99	1685
-6	0	2900	23	69.1	2.03	449	69.1	5.34	1179
-6	0	2900	24	41	1.74	328	41	4.5	852

-6	80	2300	22	27.2	2.36	429	27.2	6.01	1108
-6	80	2300	23	19.8	1.96	333	19.8	5	858
-6	80	2300	24	12.9	1.75	333	13	4.46	859
-6	80	2500	22	50.7	2.43	568	50.7	6.23	1471
-6	80	2500	23	30.7	2.04	330	30.8	5.26	855
-6	80	2500	24	19.4	1.75	332	19.4	4.49	857
-6	80	2700	22	81.5	2.43	644	81.6	6.3	1683
-6	80	2700	23	53.5	2.09	407	53.6	5.44	1060
-6	80	2700	24	30	1.79	330	30	4.6	855
-6	80	2900	22	112.1	2.39	661	112.3	6.3	1765
-6	80	2900	23	78.6	2.1	477	78.6	5.56	1254
-6	80	2900	24	46.5	1.81	327	46.5	4.72	851
-7	0	2300	22	14.3	0.82	140	14.5	2.13	368
-7	0	2300	23	10.6	0.73	128	10.7	1.91	335
-7	0	2300	24	6.9	0.72	128	6.9	1.87	335
-7	0	2500	22	40.3	1.02	205	40.5	2.72	540
-7	0	2500	23	24.6	0.82	127	24.7	2.15	334
-7	0	2500	24	13.2	0.71	127	13.2	1.86	334
-7	0	2700	22	69.1	1.11	251	69.3	2.98	668
-7	0	2700	23	45.8	0.88	144	45.9	2.34	381
-7	0	2700	24	25.8	0.7	127	25.8	1.85	334
-7	0	2900	22	98	1.13	276	98.1	3.11	754
-7	0	2900	23	69.4	0.92	175	69.5	2.49	468
-7	0	2900	24	41.2	0.71	125	41.3	1.9	332
-7	80	2300	22	27.1	1.15	166	27.1	3.03	436
-7	80	2300	23	19.9	0.84	128	20	2.21	335
-7	80	2300	24	13.1	0.72	128	13.2	1.87	335
-7	80	2500	22	51.5	1.24	226	51.7	3.31	598
-7	80	2500	23	31.2	0.91	126	31.3	2.41	334
-7	80	2500	24	19.4	0.72	127	19.4	1.88	334
-7	80	2700	22	82.1	1.26	269	82.3	3.45	720
-7	80	2700	23	54	0.95	156	54.1	2.57	414
-7	80	2700	24	30.3	0.74	126	30.3	1.96	333
-7	80	2900	22	112.2	1.24	291	112.4	3.48	799
-7	80	2900	23	78.9	0.98	187	79	2.69	500
-7	80	2900	24	46.7	0.76	125	46.8	2.04	332
-8	0	2300	22	14.7	0.33	47	14.9	0.87	125
-8	0	2300	23	10.8	0.26	43	10.9	0.68	113
-8	0	2300	24	7	0.25	43	7	0.65	113
-8	0	2500	22	40.6	0.4	69	40.8	1.07	184

-8	0	2500	23	24.8	0.29	43	24.9	0.76	113
-8	0	2500	24	13.2	0.25	43	13.3	0.65	113
-8	0	2700	22	69.4	0.43	86	69.7	1.18	231
-8	0	2700	23	46	0.31	48	46.1	0.84	129
-8	0	2700	24	25.8	0.24	43	25.9	0.64	113
-8	0	2900	22	98	0.44	97	98.2	1.24	266
-8	0	2900	23	69.6	0.33	59	69.7	0.91	159
-8	0	2900	24	41.3	0.25	42	41.4	0.66	112
-8	80	2300	22	27.1	0.43	56	27.1	1.16	148
-8	80	2300	23	20	0.3	43	20.1	0.78	113
-8	80	2300	24	13.2	0.25	43	13.3	0.65	113
-8	80	2500	22	51.8	0.47	77	52	1.28	205
-8	80	2500	23	31.3	0.32	43	31.5	0.87	113
-8	80	2500	24	19.4	0.25	43	19.4	0.66	113
-8	80	2700	22	82.3	0.49	93	82.6	1.36	250
-8	80	2700	23	54.2	0.34	53	54.3	0.94	140
-8	80	2700	24	30.4	0.26	43	30.4	0.68	113
-8	80	2900	22	112.2	0.48	102	112.4	1.38	283
-8	80	2900	23	79	0.36	63	79.1	0.99	170
-8	80	2900	24	46.8	0.27	42	46.9	0.72	112

Table S2. Initial conditions and key outputs for all models shown in Figure 4. Here Δh_w is the equivalent depth of a global ocean on the surface that would contain the mass of hydrogen that was delivered into the core in the 4.5 Gyr after the formation of Mars.

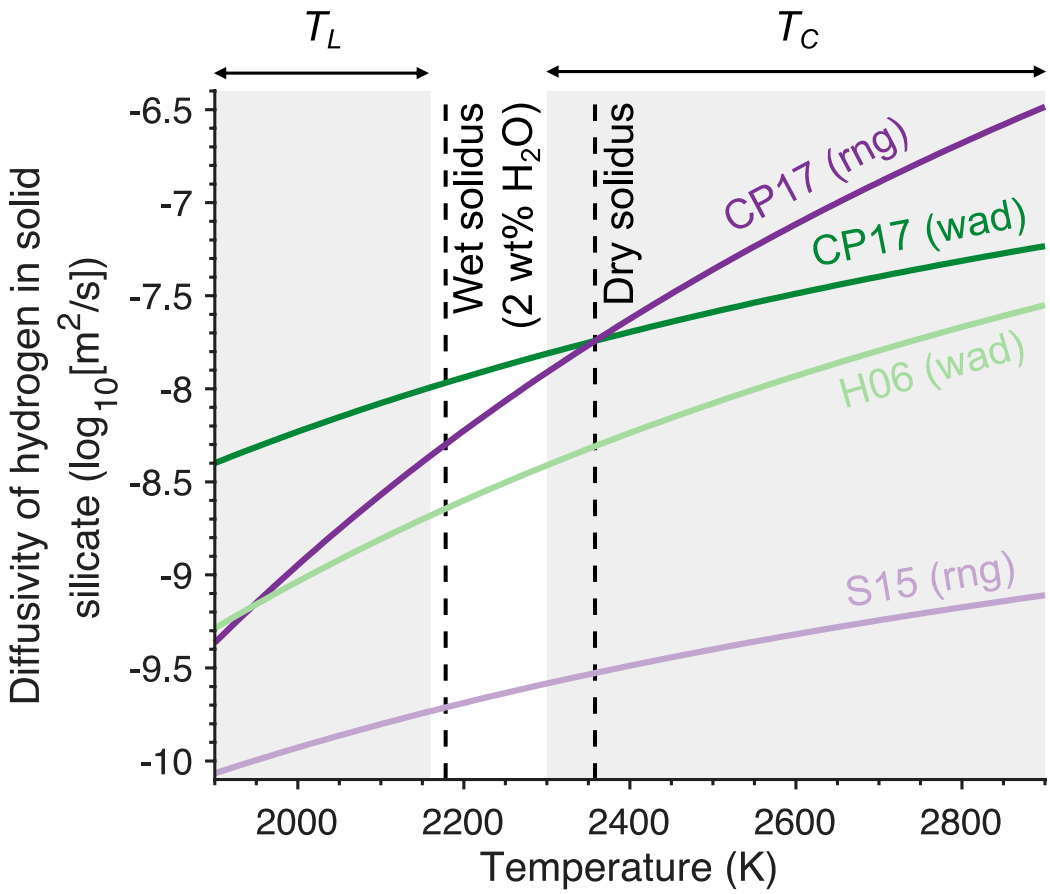

Figure S1. Recent experiments (light colors) and numerical simulations (dark colors) constrain the diffusivity of hydrogen in solid ringwoodite (purple) and wadsleyite (green). Vertical, dashed lines show the solidus of the Martian mantle at ~19 GPa assuming no water (Duncan et al., 2018) and ~2wt% of water (Litasov & Ohtani, 2007). Shaded regions show the ranges of temperatures expected for the lower mantle (T_L) and the core (T_C) in our models. Partial melting is expected in the LMBL near the CMB because temperatures there exceed the solidus, which could increase the effective diffusivity of hydrogen above these values.

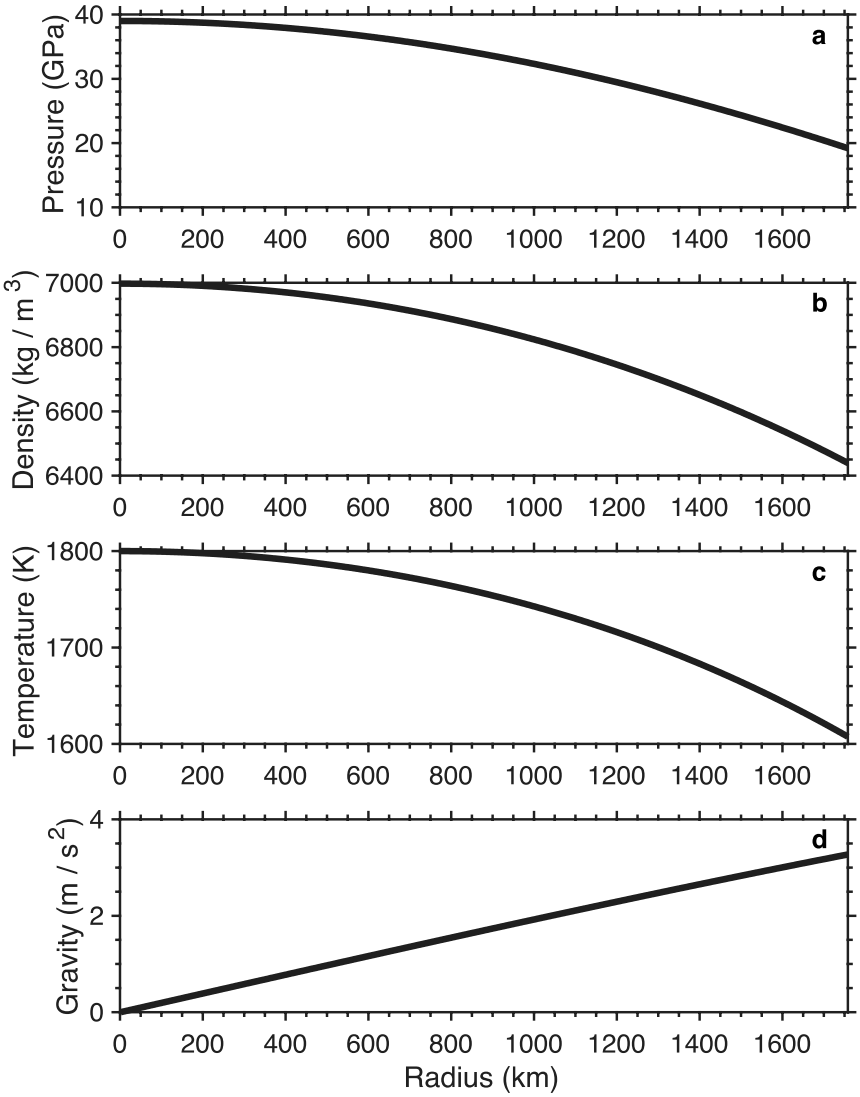

Figure S2. Our fiducial model of the core matches prior fits to geodetic constraints. We self-consistently calculate pressure **(a)**, density **(b)**, temperature **(c)**, and gravity **(d)** assuming a bulk composition of 87 wt% Fe, 12 wt% Si, and 1 wt% H and a central pressure and temperature of 39 GPa and 1800 K, respectively. We obtain a similar structure for 84 wt% Fe, 16 wt% S, and 0 wt% H—and intermediate compositions. The radius of the core is 1758 km and the CMB pressure is 19.2 GPa, which are consistent with studies that conducted detailed matches to moment of inertia and tidal Love number. We fit this density profile to a fourth-order polynomial for our energetic calculations as described in the main text (Section 2.3.1).